Master RADMEP

Master *Radiation and its Effects on MicroElectronics and Photonics Technologies* (RADMEP)

STUDY OF THE ELECTRO-OPTICAL CHARACTERISTICS OF THE LISA PHOTODIODES (IRRADIATED AND NON-IRRADIATED)

Master Thesis Report

Presented by

Alan Daniel Garcia Villagomez

and defended at

University Jean Monnet

9-10 September 2024

Academic Supervisor: Prof. Sylvain Girard

Host Supervisor: PhD Nicoleta Dinu-Jaeger

Jury Committee:

Prof. Arto Javanainen, University of Jyväskylä

Prof. Sylvain Girard, University Jean Monnet

Prof. Paul Leroux, Katholieke Universiteit Leuven

Prof. Frédéric Saigné, University of Montpellier

Erasmus+

STUDY OF THE ELECTRO-OPTICAL CHARACTERISTICS OF THE LISA PHOTODIODES (IRRADIATED AND NON-IRRADIATED)

Abstract

The Laser Interferometry Space Antenna (LISA) Mission is a project organized by the European Space Agency, in which three satellites will be sent to space with the goal of detecting gravitational waves. To achieve this, laser interferometry will be used, and to this end, photodiodes will play a very important role in converting optical signals into electrical ones. In space, semiconductor devices are exposed to radiation from many sources such as the Sun and Galactic Cosmic Rays. To better understand the expected radiation effects, electro-optical characteristics of the photodiodes must be analyzed before and after irradiation. Photodiodes developed by Hamamatsu in Japan have been tested through proton, gamma and electron irradiation and characterized more than one year ago.

A setup to study the characteristics of these photodiodes at the Observatoire de la Côte d'Azur (OCA) was implemented as many analyses were and will be performed not only on the before mentioned photodiodes, but also on future candidates for the LISA Mission. The quality of the measurements allowed us to study the annealing effects on the irradiated devices.

IV measurements showed that there is a significant effect on the photodiodes caused by proton, electron and gamma irradiation as compared to pre-irradiation measurements. Due to the amount of time between measurements, annealing effects were observed for electron irradiation although no annealing was detected for proton irradiation. The gamma ray irradiated photodiode had undergone an annealing process, and further annealing effects were not observed on it.

CV measurements showed a slight increase in capacitance after irradiation, but differences were so low and within standard deviations between the 4 quadrants of each photodiode, that conclusions regarding the radiation effects cannot be drawn, and it is even possible to say that no radiation effects were observed on the capacitances of the photodiodes.

Experimental damage factors were obtained from the dark current values, for proton and electron irradiated photodiodes, showing once again no annealing from proton irradiation while electron irradiation did present annealing. A slight tendency is observed in which the photodiode size affects the damage factor, being lower at larger photodiode diameters. These damage factors were used to obtain the Non-Ionizing Energy Loss (NIEL) of each measurement, by using the NIEL scaling approach, showing a tendency from proton irradiated photodiodes to have higher coulombic interactions at higher energies as compared to nuclear interactions.

Acknowledgements

First and foremost, I would like to express my gratitude to my supervisor PhD Nicoleta Dinu-Jaeger, for giving me the opportunity to contribute to the LISA Mission, as well as for her commitment and valuable feedback. Her assistance and insight made this work possible.

Second, I would like to thank PhD Paul Colcombet. The detailed explanations on technical matters, as well as very interesting discussions regarding the observed phenomena and data comparison allowed conclusions to be drawn and further work to be done.

I would like to thank all the professors from the different universities, from which I not only acquired technical knowledge, but also passion for the topics that were covered. I would like to thank Prof. Sylvain Girard for his assistance not only with technical matters during this internship but also administrative and personal ones.

A special thanks goes to Leena Mattila and Amelie Genvrin for their assistance with the many administrative and bureaucratic matters that made this master's degree possible. Their willingness to help at every step of the way is deeply appreciated.

I want to thank all my classmates for all the great memories and experiences shared together throughout this adventure. A special thanks to my friend Geoffrey for his support and enthusiasm, always keeping a positive attitude regardless of the situation.

Finally, I would like to thank my family, as this accomplishment is as much theirs as it is mine.

Table of contents

Table of Figures

Table of Tables

1. Introduction

1.1 About Gravitational Waves

As early as in the 19th century, English mathematician and physicist Olivier Heaviside started theorizing about gravitational waves (GW). Later in 1905, such theories became reinforced by French physicist Henri Poincaré when he pointed out that GW should propagate at the speed of light. On 1916, after publishing about General Relativity, Albert Einstein predicted the existence of GW, deduced the wave equation that satisfied General Relativity and found that GWs actually do travel at the speed of light. Albert Einstein set the basis upon which the scientific community would work upon the GWs. As an analogy of an accelerating electrical charge produces electromagnetic waves, so are GW generated by the acceleration of masses [1]. The study of GW is fascinating among other things, because it represents an unexplored non-electromagnetic spectrum.

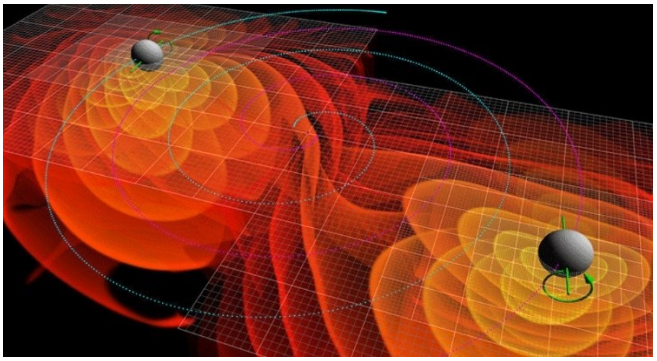

Figure 1: Simulation of gravitational waves. Courtesy of C. Henze/ NASA Ames Research Center.

Gravitational radiation, similar to electromagnetic radiation was first observed from the orbital decay of the Hulse-Taylor binary pulsar, from which the physicists Russell A. Hulse and Joseph Taylor Jr. received the Novel Prize in Physics in 1993 [2]. Pulsar timing is a method to study neutron stars by calculating pulse arrival times. With its high precision the orbits of pulsars in binary systems can be measured. Due to its high precision and the orbital decay detected, it was said to be an "indirect GW discovery" [3].

To measure GW, a method that is able to measure changes in distance down to the nanometer scale must be used. Laser interferometry makes use of the wavelength of light to measure changes in distance. Such a precision level is used in many fields of modern technology, such as dimensional and surface metrology, which is an alternative to scanning probe microscopy with the advantage of having no contact with the samples, so they don't get damaged [4]. In contrast with its applications in microscopy, its use in astronomy for GW proves the versatility of this technology.

Efforts have been made to study GW by developing large scale laser interferometers, since this technology allows us to measure distances in the range of nanometers down to picometers. Installations such as LIGO (Laser Interferometry Gravitational-Wave Observatory) and VIRGO are based on the Michelson interferometer and have set the basis for future study in the field [5]. In fact, they are gigantic ground-based Michelson

Interferometers, of 4 and respectively 3 km arm's length. The first ever direct detection of a GW was done by LIGO in 2015, where a transient GW signal with a frequency ranging from 35 to 250 Hz was detected with a peak GW strain of 1.0 x 10^{-21} [6].

The Earth's gravitational gradient (seismic wall) limits the LIGO and VIRGO detectors to detect low frequency GW. Density fluctuations on the Earth's surface produced near the location of the mirror of the interferometers are the dominant source of gravity gradients which affect the measurement of GW [7]. To overcome this limitation and perform measurements in the ranges of 0.1 mHz to 1 Hz, the LISA (Laser Interferometry Space Antenna) space mission concept, representing a GW observatory in space was born in the years 1980 with the goal of detecting low frequency gravitational radiation. Massive black holes and binary systems will be able to be detected with LISA, and the number and distribution of thousands of binary systems containing compact stars will be able to be determined [8].

1.2 LISA Mission

LISA is a Mission of the European Space Agency (ESA), in collaboration with the National Aeronautics Space Administration (NASA) and Space agencies and scientific institutes from 14 European countries. The instrument consists of three satellites, shaping an equilateral triangle, equidistant from each other at a distance of 2.5 million km and following the Earth at about 50 million km. The launch is scheduled for 2035. The orbit and relative position with Earth are shown in Figure 2.

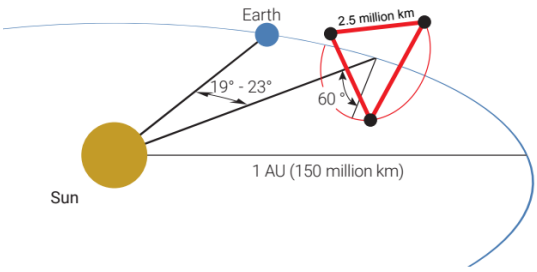

Figure 2: LISA Mission satellites' orbit.

The LISA mission uses a variation of the Michelson interferometer, called transponder mode. To this end, one laser beam of ~ 1.5 W optical power is sent from one satellite to the far one. Because of the long distance between satellites and the divergence of the beam, the optical power received by the far satellite is only ~500 pW. Therefore, a second laser beam of 1.5W optical power and phased locked to the received beam is sent back to the first satellite.

Modern laser technologies at 1064 nm wavelength are used for LISA mission [9]. However, the laser frequency noise remains one of the most important noise sources of the LISA instrument. To this end, a post-processing technique called Time Delay Interferometry (TDI) has been developed [10]. By making time-shifting and linear combination of the interferometric measurements from the three LISA arms, the TDI allows to form virtual equal arm Michelson interferometers and to reduce the laser frequency noise by few orders of magnitude.

The two laser signals exchanged between the satellites allow to detect ~pm relative distance variation between two tests masses in free falling, installed at the end of each interferometric arm. These interferometric optical signals will be detected by photoreceivers containing photodiodes which will allow the data processing. The study of the LISA photodiodes' main electrical characteristics (leakage current and capacitance) under the LISA radiation environment represents the main subject of the present thesis, that will be developed in the following chapters.

1.3 Radiation Effects on electronics

When travelling through space, the LISA Mission satellites will be exposed to radiation coming from various sources, without the protection of Earth's magnetic fields. Intermittent solar emissions, Galactic Cosmic Rays coming from a faraway supernova and Radiation Belts trapped by a planet's magnetic field contain highly energetic particles such as protons, electrons and heavy ions, which can impact the various components in the satellites, seriously damaging them and affecting their performance. Due to the orbit the LISA Mission will face, the main radiation sources will be the Sun and the Galactic Cosmic Rays. On average, solar wind from the Sun is composed of mostly protons (95%), alpha particles (4%) and minor ions such as carbon, nitrogen and oxygen. Earth's radiation belts (Van Allen belts) will not play a role in the degradation of the LISA photodiodes, due to the large distance between Earth and the satellites (about 50 million km) [11].

Semiconductor materials are made of crystal structures and, as their name suggests, can be conductors or non-conductors, depending on the doping they have been through, in which impurities are added with elements that have either 5 or 3 electrons in their valence band. When they are doped with the former, they are said to be n-type semiconductors, and they have now a free electron from the doping element. Similarly, when they are doped with the latter, they become p-type semiconductors, and they lack one electron or have an extra hole. Both n-type and p-type semiconductors have much higher conductivity than intrinsic semiconductors, and they can be used to create special electronic components such as transistors, diodes and photodiodes [12].

Depending on the type of radiation particle that causes the interaction, we may have different effects or phenomena happening. If photons impact an atom, they can cause Rayleigh scattering, Photoelectric effect, Compton scattering and pair production. Depending on the cross section of the impact and the photon energy some effects may be more predominant than others. Rayleigh scattering and photoelectric effect are more dominant at low energies (< 1 MeV) while at high energies pair production is predominant (> 1MeV). Compton scattering can be seen throughout all energy ranges [13]. The main effects of photons in matter and their frequency ranges are shown in Figure 3.

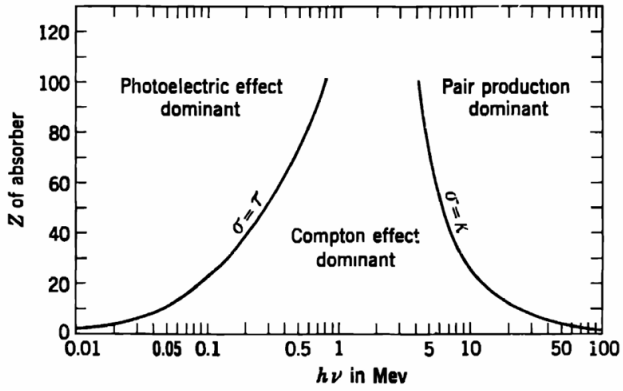

Figure 3: Energy ranges of photon-matter interaction effects. Extracted from [14].

When a heavy ion impacts an atom, it can have an elastic or an inelastic interaction with it. Electrons and positrons can also have elastic and inelastic interactions, but they can also cause Bremsstrahlung emission, Cerenkov emission and Positron annihilation. So far, all the interactions discussed are based on the fundamental electromagnetic force. When nucleons such as protons and neutrons interact with matter, it is the Strong force that causes the interaction. Such an interaction can be elastic and non-elastic. The elastic interactions do not change the nature or excitation energy of the initial particles. The kinetic energy is not conserved in non-elastic interactions, and nuclear reactions take place, where there is a production of secondary particles [15].

When a highly energetic particle interacts with a semiconductor, most of its energy goes to the excitation of electrons, creating an electron-hole pair. In semiconductors and metals, these electron-hole pairs recombine or move by drift and diffusion, but in insulators things are a bit different. If there is an electric field applied to the material, the high mobility of electrons will allow them to be swept away even through the insulator, but since the mobility of holes is much lower, they will depend on localized shallow traps in the insulator to travel by hopping, and once they reach the interface between the insulator and a semiconductor material, they get stuck in interface traps. These trapped positive charges affect the performance of semiconductor devices [16]. Such a process can be seen in Figure 4. An incident electron with energy *hv* interacts with an insulator (in this case SiO_2) with a band gap E_G.

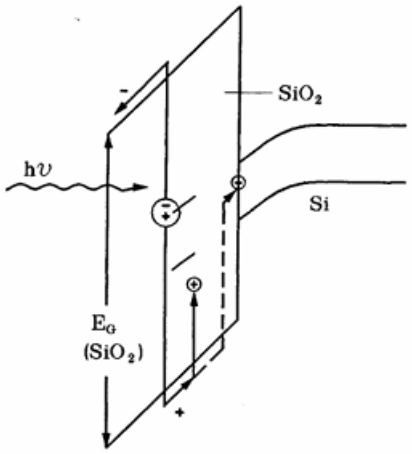

Figure 4: Generation of an electron-hole pair, trapping of a hole. Extracted from [15].

Radiation effects on electronics can be of two different natures: cumulative or single events. Cumulative radiation effects are caused by the degradation of electronic devices, when they have been exposed to radiation over a period of time, while single events happen when a single highly energetic particle damages or causes malfunction in the electronic device. Cumulative radiation effects are Total Ionizing Dose (TID) and Displacement Damage Dose (DDD). Single Event Effects (SEE) can be destructive or non-destructive, and depending on the type of interaction they can be single event upsets, single event latches, single event gate rupture, single event burnout, etc. Both TID and SEE are the result of ionizing radiation while DDD is caused by a non-ionizing interaction [17].

TID is caused by holes accumulated over time in semiconductor interface traps, while SEEs are caused by the drift and diffusion of electron-hole pairs in semiconductor materials. DDD works by causing atomic displacement damage, by ejecting nuclei of atoms, creating interstitials and vacancies in the semiconductor crystal lattice. Radiation cumulative effects can cause carrier generation, carrier trapping, recombination centers, tunneling effects, etc. all of which affect the performance of, in this case, photodiodes which are exposed to radiation.

The motion of vacancies and interstitials in a semiconductor material can be affected by the physical conditions in which it is present. A higher temperature can affect this motion and aid the crystal in re-structuring to find a more stable configuration. Annealing is a heat treatment which alters the chemical and physical properties of a material. An early definition for semiconductors indicated that it was due to the annihilation of vacancies and interstitials, but other crystal defects are also affected by annealing [18].

1.4 Master Thesis Environment

The ARTEMIS (Astrophysique Relativiste, Théories, Expériences, Métrologie, Instrumentation et Signaux) is one of the three laboratories of the Observatory Cote d'Azur, situated on Mont Gros site at Nice. The ARTEMIS scientific theme is the physics of the GW. To this end, ARTEMIS team focuses, among other things, on the technologies such as lasers and their stabilization in frequency and power, laser interferometry

techniques and photodetectors for both ground and space detectors dedicated to the detection of GW

1.5 Objectives and thesis structure

The objective of the current thesis is to measure the radiation effects of proton, electron and gamma irradiation on candidate photodiodes for the LISA Mission. The specific objectives are as follows:

- Development and calibration of the testbench for the measurement of Current Voltage (IV)/ Capacitance Voltage (CV) characteristics of the photodiodes, including temperature control with a Climatic chamber.
- Measurements of the IV and CV characteristics at different temperatures, ranging from 20 to 50 degrees Celsius on specific photodiodes developed for the LISA Mission; the set of the studied photodiodes includes non-irradiated ones (e.g. references) and irradiated with protons, electrons and gamma rays.
- Specific analysis of annealing effects over one year time between irradiation moments and actual measurements.

This document will first describe an introduction explaining the context of the thesis, and some basic theoretical background regarding the LISA Mission and the radiation effects on semiconductor materials. Then, the development and the calibration of the test setup will be described, as well as the methodology followed to perform the measurements with this setup.

Then, the results of the measurements will be described, and analysis of the obtained data will be discussed. After that, conclusions will be drawn from the results and future work in the field will be mentioned.

2. Theoretical background

2.1 Gravitational waves detectors and need for photodiodes

GWs are ripples in spacetime caused by the acceleration of massive objects, such as merging black holes or neutron stars. As mentioned previously, the method to detect GWs is by using laser interferometry to be able to detect sub-picometer distance variations.

Michelson interferometry works by making use of a beam splitter, which splits a light source into two paths. Each of the light beam's travels to a distant mirror which reflects the beam back into the splitter which combines their amplitude and depending on the phase shift the two beams can cause constructive or destructive interference. The basic schematic of a Michelson Interferometer is shown in Figure 5.

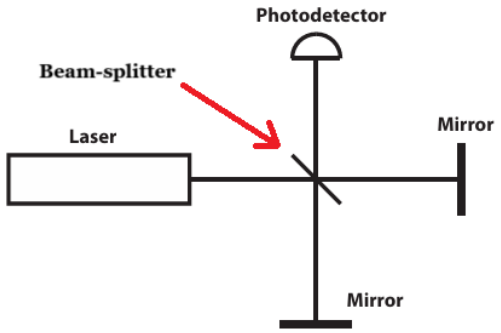

Figure 5: Michelson interferometer schematic. Adapted from [19]

LIGO makes use Michelson interferometry to detect GWs with strains smaller than one part in 10^{21} focusing on the amplitude rather than the power of the GW, so the volume of proved space increases as the cube of the strain sensitivity. A basic schematic showing the way GWs are detected by LIGO is shown in Figure 6. A GW with a strain amplitude h distorts a ring of test masses into an ellipse, stretched into one direction in a half of the cycle and stretched in the other direction at the other half. The distortion caused by this oscillation can be measured with laser interferometry, as the phase shifts of the light are detected as intensity modulations at the photodetector (indicated in green in Figure 6).

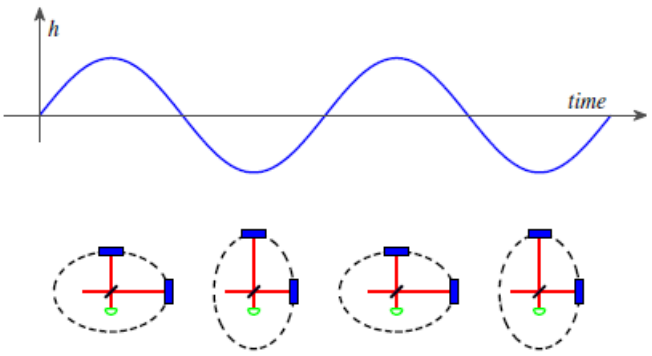

Figure 6: GW detection method using a Michelson Interferometer. Extracted from [20]

Laser interferometers based on Earth's ground use homodyne detection schemes, i.e., the received laser and the reference oscillator have the same frequency. For the LISA mission, the received laser, the transmitted laser and the reference laser have different frequencies. This is called Optical Heterodyne Interferometry and is simpler to implement as there is a Doppler Effect caused by the change in the distances between the LISA mission satellites due to orbital mechanics. Such a Doppler Effect will cause the emitted and received laser to have different frequencies, which heterodyne interferometry already makes use of. Also, a heterodyne scheme makes calibration between registered signal phase and the amplitude of the GW easier [21].

Interferometric measurements allow to detect tiny variations of distance between two free-fall masses (i.e. undisturbed by forces other than gravity) which reflect light and behave as the mirrors in the interferometric measurement. Such variations are caused by GWs. The detection of the interferometric signals is done using photoreceivers, that convert the optical signals into electrical amplified signals.

The photoreceivers are made of three important elements: a photodiode which converts the optical signal into electric current, front-end electronics which amplifies and converts the electrical current into voltage by using a trans-impedance amplifier (TIA), and a mechanical enclosure for the components. Since in this project the objective is to analyze the electro-optical characteristics of the photodiodes, they will be discussed next.

2.2 Specifications of photodiodes for the LISA Mission

When n-type (excess electrons) and p-type (excess holes) semiconductors are joined together, the charge carriers interact with each other at the junction. The excess electrons from the n-type material fill the holes from the p-type material, leaving a region without excess electrons and excess holes called the depletion region. The part of the depletion region located in the p-type material has a negative charge since all the holes are covered by electrons, and the side of the depletion region located in the n-type material has now positive charge since all the excess electrons migrated to the p-type material. The width of the depletion region depends on the electric field between the materials at the junction, and there is an intrinsic electric field caused by the excess electrons of the n-type material and the excess holes of the p-type material. The p-n junction can be observed in Figure 7.

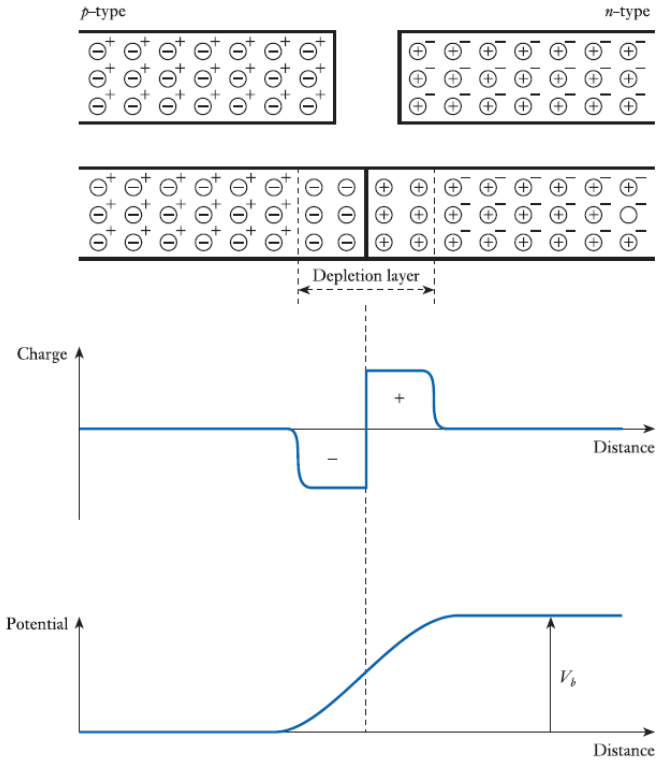

Figure 7: p-n junction and depletion region. Extracted from [22]

If an external electric field is applied to a p-n junction, it can increase or reduce the width of the depletion region depending on the polarity. If the p-type side of the junction is connected to the positive polarity of an external electric field, the negative charge in the depletion region gets pushed and decreased in size, such that the potential barrier to get to the other side of the junction gets decreased, and conductivity is made possible.

If the negative polarity of the electric field is applied to the p-side of the p-n junction, this only increased the negative charge of the depletion region of the p-type side and therefore the potential barrier increases, and conductivity decreases, even reducing the diffusion current along the junction. The current through a p-n junction can be calculated with the expression shown in equation 2.1:

$$I = I_s(e^{\frac{eV}{\eta kT}} - 1) \qquad 2.1$$

Where I is the current through the junction, I_s is the reverse saturation current and it's a constant, e is the charge of an electron, V is the applied voltage (negative for reverse bias), k is Boltzmann's constant, T is the absolute temperature and η is a constant called the emission coefficient between 1 and 2, where it approximates 1 when it's an ideal diode and 2 when it's less ideal.

When light falls on a pn junction, a voltage is produced, generating power from light. Photodiodes make use of this principle to measure light intensity. A small forward voltage is enough to make the device conduct electricity. Although at a reverse bias, only a small reverse current goes through the device until the device reaches a critical voltage

called the reverse breakdown voltage. Photodiodes work at this reverse bias, as the amount of current depends on the intensity of the light received. This can be seen in Figure 8.

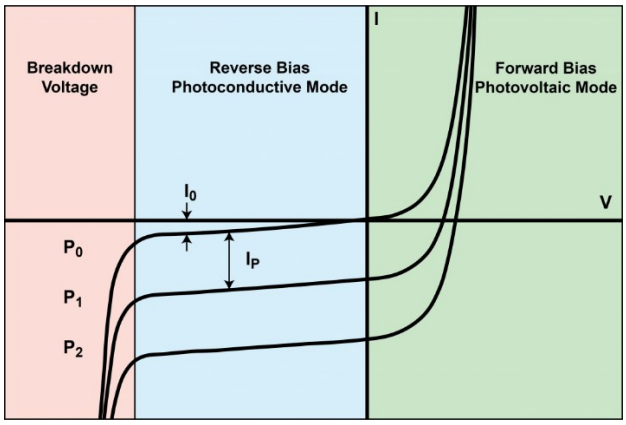

Figure 8: I-V regions in a photodiode. Extracted from [23].

At reverse bias, the p-type and the n-type semiconductors are separated by a depletion region, resembling a capacitor. Depending on the reverse bias voltage, the width of the depletion region can change, thus changing the capacitance of the diode. Capacitance can be calculated with equation 2.2:

$$C = \frac{\varepsilon_0 \varepsilon_r A}{d} \qquad 2.2$$

Where C is the capacitance, ε_0 is the permittivity of free space, ε_r is the relative permittivity of the dielectric material, A is the area of the conducting plates (in this case, the n and p-type semiconductors) and d is the distance between the conducting plates. The dependency of the capacitance with respect to the reverse bias voltage applied follows equation

$$C = \sqrt{\frac{qN\epsilon A^2}{2(V + V_{bi})}} + C_0 \qquad 2.3$$

Where C is the capacitance, q is the charge of an electron, N is the doping, ϵ is the absolute permittivity of the material, A is the photodetector area, V is the applied voltage, V_{bi} is the built-in voltage and C_0 is the additional capacitance.

The equivalent circuit of a photodiode can be seen in Figure 9. The parts of this equivalent circuit are the photocurrent I_P, the ideal diode, a parallel shunt resistance R_{SH} which is infinite for an ideal photodiode, a parallel capacitor C_J representing the junction capacitance, a series resistance R_S caused by the cables and connections, and a load.

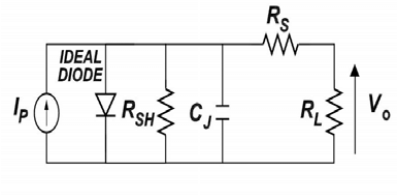

Figure 9: Equivalent circuit of a photodiode. Extracted from [24].

Making use of this model will help us understand better the behavior of the LISA photodiodes and the change of their characteristics under irradiation.

2.2.1 Special types of InGaAs photodiodes

There exist particular types of photodiodes with special characteristics. One of them is the PIN (p-type, intrinsic, n-type) photodiode, in which a layer of intrinsic semiconductor material is put between the n-type and the p-type semiconductors. This layer is highly resistive and increases the electric field strength of the device. It also acts as an extension to the depletion region, making it wider, decreasing its capacitance and increasing the response speed. The PIN photodiode is illustrated in Figure 10.

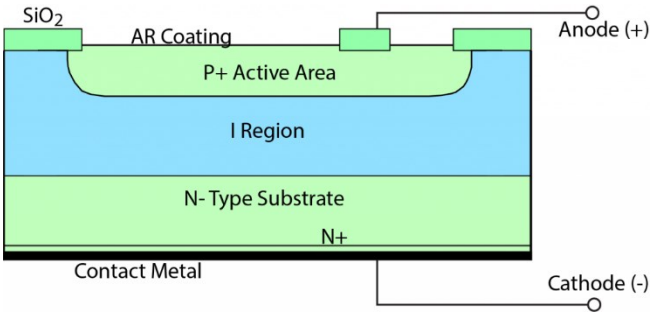

Figure 10: PIN photodiode. Extracted from [23].

If an additional intrinsic layer is added to a conventional PIN photodiode, the junction capacitance can get reduced while conserving the advantage of the response speed. A thick photodetector has a long transit time (i.e. the time it takes for the carriers to go from the intrinsic region to the electrode surfaces) because the charge carriers are moving at saturation velocities. But a thin depletion region will have a high capacitance, which affects the constant of detection, causing a slow response. Therefore, capacitance requires a thick intrinsic layer while transit time requires a thin layer.

Indium Gallium Arsenide is a ternary semiconductor with chemical composition $In_xGa_{1-x}As$ for which the band gap can be modified. Depending on the composition of x, the lattice parameter a can go from 5.65 Å for GaAs (with a band gap of 1.435 eV) to 6.06 Å for InAs (with a band gap of 0.35 eV) and the wavelength it works with can be modified to be between 0.85 µm and 3.6 µm. Only the chemical composition $In_{0.53}Ga_{0.47}As$ can be lattice matched for InP, allowing its growth on InP as substrate, whereas no other compositions can be lattice matched to either InP or GaAs as to allow direct growth [26].

By making use of an InGaAs absorption layer and an InP buffer drift layer in the depletion region, electrons must travel across both layers while holes only must travel

across the InGaAs absorbing layer, due to their carrier velocity. By changing the design parameters of the device, the transit times for electrons and holes can be optimized. Dual Depletion Region (DDR) thus reduces capacitance without increasing carrier transit time [25]. The DDR photodiode structure can be seen in Figure 11.

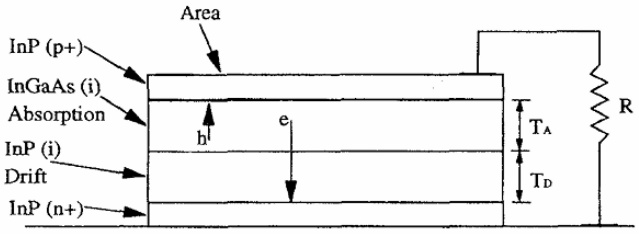

Figure 11: Dual Depletion Region Photodiode. Extracted from [25].

The photodiodes used for the LISA Mission are DDR photodiodes, benefiting from the reduced capacitance and improved carrier transit time that such a design offers.

2.2.2 Radiation effects on InGaAs photodiodes

InGaAs photodiodes based on a PIN configuration have been tested under proton irradiation at 3 MeV with fluences of 1×10^{11}, 1×10^{12} and 1×10^{13} cm^{-2} and showing good radiation resistance when used at 850 nm but their capacitance increases which might play a great role at the TIA, since jitter caused by this increase in capacitance can cause a sensitivity penalty [27]. InGaAs has also been used to develop radiation-resistant solar cells, showing that the number In-P bonds with InGaP, InGaAsP and InGaAs affect the degradation caused by radiation, therefore the higher the number of In-P bonds, the higher the radiation resistance [28].

There is a particular phenomenon that causes a deviation from the ideal diffusion model in p-n junctions, caused by the generation and recombination of carriers caused by generation and recombination centers located in the depletion region. Such recombination centers have received the name of Shockley-Read-Hall recombination centers (SRH) [29].

It has been reported that for $In_{0.53}Ga_{0.47}As$ photodiodes, 1 MeV electron irradiation produces a defect level in the band gap, which was denoted E2, located 0.29 eV below the fermi level (i.e. Ec-E2 = 0.29 eV). This defect acted as a generation center in the photodiode. Further analysis with deep level transient spectroscopy showed that there is a logarithmic decay of radiation induced generation current caused by isothermal annealing of the E2 defects, for a time period of 2 weeks. The most likely defects caused by 1 MeV electrons are Frenkel (interstitial-vacancy) pairs, and recombination seems to be the annealing mechanism [30].

In another study, $In_{0.53}Ga_{0.47}As$ photodiodes were irradiated with protons with energies ranging from 14.4 to 62 MeV and at 291 and 250 K temperatures. When protons interact with a particle, the interaction is governed by the fundamental strong force, instead of the electromagnetic force which dominates the interactions of electrons with atoms. The interaction of protons with atoms can cause elastic and non-elastic interactions. In the elastic interactions, vacancies and interstitials are generated in the crystal lattice of the semiconductor, causing displacement damages, whereas non-elastic interactions can

cause nuclear reactions in which alpha particles can be emitted. In both of these interactions, a primary knock-on atom (i.e. the first atom interacting with the incoming particle) can acquire a lot of energy from the interaction thus behaving like a new incoming particle in the lattice. This primary knock-on atom can interact with other atoms in the lattice, causing further damage such as ionization, displacement damage or even nuclear reactions. The Non-Ionizing-Energy-Loss (NIEL) is the amount of energy an incoming particle loses due to non-ionizing interactions in a lattice, and it quantifies the displacement damage per unit path. At high reverse bias voltage, NIEL scaling might not provide the most accurate results. When protons with energies higher than 10 MeV interact with a lattice, complex clusters of defects are created, but for incoming particles with energies lower than 10 MeV, point defects are dominant. This is illustrated in Figure 12 for Silicon.

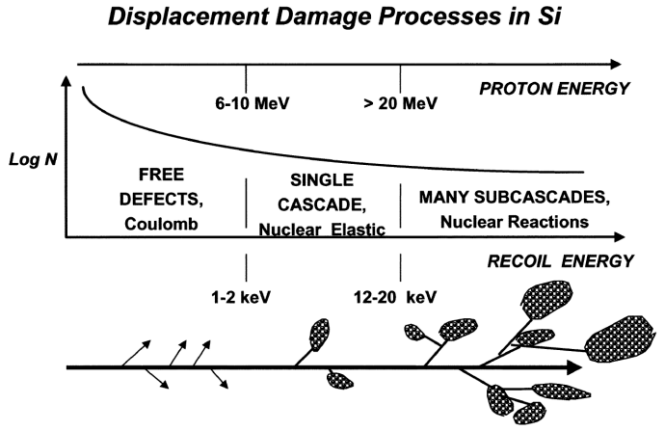

Figure 12: Proton-particle interaction dependency with energy [31]

At high electric fields, the complex defect clusters are more sensitive to the Electric Field Enhancement (EFE) i.e. electric field enhancement of the thermal generation rate. But at low reverse bias, the dark current related damage rate (DCDR) follows the NIEL scaling approach, which is a method to scale the expected device degradation from one radiation type to another [32].

2.3 Radiation requirements on LISA Mission photodiodes

The LISA Mission radiation requirements are shown on Table 2.1. The table shows the expected radiation conditions the Mission will face in the case of an extension of its duration (i.e. a total duration of 12.5 years). The Non-Ionizing-Energy-Loss (NIEL) for InGaAs, the Displacement Damage Dose (DDD), the Displacement Damage Equivalent Fluence for monoenergetic spectra (DDEF), the Total Ionizing Dose (TID) with the respective Aluminum shielding thickness are all presented. These values were obtained based on the NASA GSFC ESP model, used by the LISA mission, in which the assumptions include maximum time during a solar maximum period within an 11 year cycle with a 4 year minimum, having negligible impact from solar minimum periods. Based on the obtained mission cumulative fluence with respect to the Proton energy, based on the previous assumptions, the requirements were established.

Table 2.1: LISA Mission radiation requirements. Extracted from [33].

Particle	Energy [MeV]	NIEL [MeV.cm²/g (InGaAs)]	DDD [MeV/g (InGaAs)]	DDEF [#p/cm²]	TID [krad]	Al shield thickness
Protons	10	6.59×10^{-3}	5.10×10^{-8}	7.74×10^{10}	78.2	3 mm
	20	4.69×10^{-3}	5.10×10^{-8}	1.09×10^{11}	55.3	3 mm
	60	3.69×10^{-3}	5.10×10^{-8}	1.38×10^{11}	29.6	3 mm
Gamma					30.6	3 mm

The DDD and DDEF values are based on NIEL for an infinitesimal sensitive target layer, without considering its thickness or any layer covering it. The TID values for protons were not derived from the stopping power in line with the TNID, the DDEF or the NIEL because there was no available data for InGaAs at the NIST PSTAR database, so instead a Geant4 simulation was performed, assuming a 300 μm sensitive layer since there is no information regarding the technology of the photodiodes as they are developed by a private company (Hamamatsu). Also, as there were no InGaAs NIEL tables available, the Summers GaAs tables were assumed. The LISA Mission requires that the photodiodes provide a dark current of less than 1 μA. Overall input current noise for the quadrant photo-receivers must be less than 2 $pA/\sqrt{Hz}$ over a bandwidth of 3 to 30 MHz. Based on this, the required capacitance from the photodiodes is less than 10 pF per quadrant [33].

3. Methodology

3.1 Devices description

The photodiodes to be analyzed for this project were a special design of DDR InGaAs quadrant photodiodes produced by Hamamatsu company in Japan, with photosensitive diameters of 1 mm, 1.5 mm and 2 mm. These photodiodes are designed to convert an optical wavelength of 1064 nm into photocurrent. They are designed to have a large photosensitive surface while having a low capacitance and low noise. These photodiodes are made of Indium-Gallium-Arsenide with proportions $In_{0.53}Ga_{0.47}As$.

The LISA photodiodes are quadrant photodiodes, in which each quadrant has its own anode while sharing the same cathode with the other quadrants. This is illustrated in Figure 13.

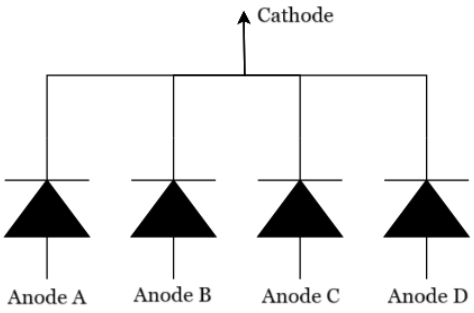

Figure 13: Quadrant Photodiode schematic

Each quadrant is separated from the other by a gap of 20 μm. For convention, the quadrants will be labelled A, B, C and D as shown in Figure 14.

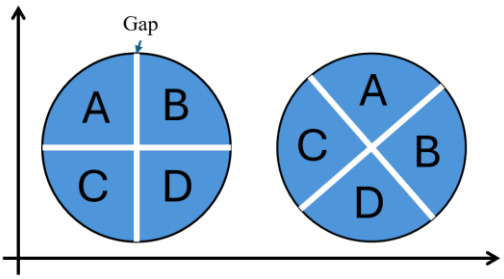

Figure 14: LISA Mission quadrant photodiodes top view diagram.

Five samples of each photodiode size were used for different irradiation tests, and the photodiodes were numbered from 1 to 5, being 1 of each size the reference photodiode and thus not irradiated. The photodiodes were encapsulated in TO-5 metal semiconductor standard packaging. The samples can be seen in Figure 15.

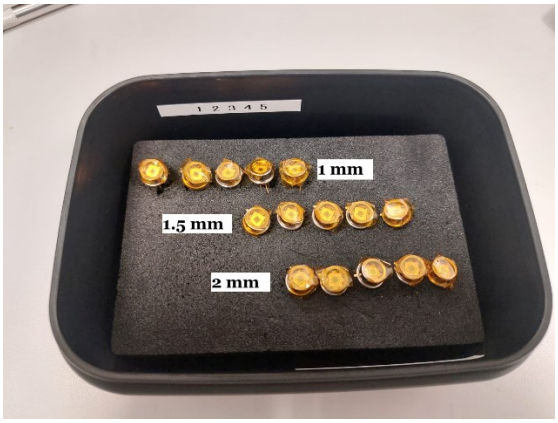

Figure 15:G6849 Quadrant Photodiodes used for irradiation tests

The parameters for the photodiodes can be seen in Table 3.1.

Table 3.1: Test photodiodes characteristics

Characteristics	**Photodiode**		
Diameter [mm]	1	1.5	2
Cross gap [µm]	20	20	20
Sample number	5	5	5
Standard Vbias [V]	5	5	5
Full depletion voltage [V]	≈3.5	≈3.5	≈3.5

The photodiodes described previously were irradiated in three different irradiation campaigns at different facilities:

- Electron irradiation took place at the AXEL facility at ONERA in Toulouse, France, equipped with two Van de Graaff accelerators connected to the MIRAGE target chamber [34].
- Gamma irradiation took place at the MEGA facility at ONERA in Toulouse, France, making use of a ionization chamber with a Co^{60} gamma [35].
- Proton irradiation took place at the Centre Antoine Lacassagne (CAL) in Nice, France, at the MEDICYC facility, equipped with a 65 MeV isochronous cyclotron, which has a R&D beamline for radiation hardness tests.

Each irradiation type applied to each photodiode is illustrated in Table 3.2.

Table 3.2: Irradiation conditions for test photodiodes

Irradiation type	**Energy**	**Size**		
		1 mm	1.5 mm	2 mm
Reference		N°1	N°1	N°1
Protons	20 MeV	N°2	N°2	N°2
	60 MeV	N°3	N°3	N°3
Electrons	0.5 MeV	N°4	N°4	N°4
	1 MeV	N°5	X	N°5

Gamma	1.25 MeV	X	N°5	X

At the end, the Fluence, TID, DDD for each irradiation type are displayed in Table 3.3.

Table 3.3: TID and DDD applied on QPDs

Particle type	Energy [MeV]	Fluence [p/cm²]	TID [krad]	DDD [MeV/g]
Proton	20	1×10^{12}	237	4.8×10^{9}
	60	1×10^{12}	104	3.6×10^{9}
Electron	0.5	5×10^{12}	105	3.4×10^{7}
	1	5×10^{12}	100	9.7×10^{7}
Gamma	1.25		237	$\approx 1 \times 10^{7}$

Irradiation took place through many stages for each type, for each device, and the final cumulative fluence for both 20 MeV and 60 MeV protons was 1×10^{12} p/cm², for 0.5 MeV and 1 MeV electrons it was 5×10^{12} e/cm² and for 1.25 MeV Gamma rays the cumulative dose was 237 krad [36].

Based on the irradiation type and the photodiode size, a number was assigned to each photodiode for their analysis. The number assignment is shown in Table 3.4.

Table 3.4: Photodiode number assignment based on size and irradiation type and energy

Photodiode number	Size [mm]	Irradiation type	Irradiation energy [MeV]
1001	1	Reference	
1002	1	Proton	20
1003	1	Proton	60
1004	1	Electron	0.5
1005	1	Electron	1
1501	1.5	Reference	
1502	1.5	Proton	20
1503	1.5	Proton	60
1504	1.5	Electron	0.5
1505	1.5	Gamma rays	
2001	2	Reference	
2002	2	Proton	20
2003	2	Proton	60
2004	2	Electron	0.5
2005	2	Electron	1

3.2 Measurement setup

For the analysis of the photodiodes, Capacitance-Voltage (C-V) and Current-Voltage (I-V) measurements must be performed, ensuring that parasitic impedances are avoided or compensated as much as possible. Both of them will be discussed separately.

3.2.1 Capacitance-Voltage (C-V) setup

In order to measure accurately the capacitances of the device under test, parasitic impedances and capacitances of the setup must be avoided or compensated as much as possible. The higher the frequency that is being handled, the bigger the effect such parasitics have on the measurements.

For the C-V measurements, the device Keysight Impedance Analyzer E4990A was used along a range of frequencies from 20 Hz to 30 MHz, as 30 MHz is the working frequency of the photodiodes in the LISA Mission. This device measures impedance by using the auto-balancing-bridge method as shown in Figure 16. To measure the complex impedance of a Device Under Test (DUT), we need to know the voltage applied to the DUT as well as the current going through the DUT. This is done by using a signal source, a voltmeter and an ammeter. Both the voltmeter and the ammeter will measure the vectors containing the magnitude and the phase of the signal voltage and the current respectively. In Figure 16 the ammeter is replaced by an operational amplifier with a negative feedback loop.

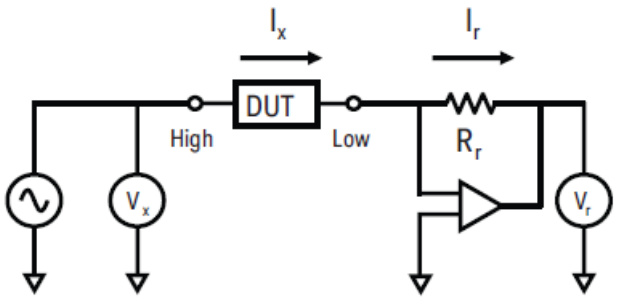

Figure 16: Auto balancing bridge method. Extracted from [37]

The impedance measurement with this setup becomes then obtained with the following formula:

$$Z_x = \frac{V_x}{I_x} = R_r \frac{V_x}{V_r}$$

Where Z_x is the impedance of the DUT, V_x is the signal voltage applied to the DUT, I_x is the current going through the DUT, R_r is the range resistor and V_r is the I-V converter output voltage [37].

The auto balancing bridge method uses 4 terminals: Hc, Hp, Lp and Lc. Hc applies a measurement signal with controlled frequency and amplitude, Hp detects the DUT's Hi potential with an extremely high input impedance as to allow accurate detection with low voltage drop. The Lp terminal detects the Lo potential, and the Lc terminal converts the current flowing into the DUT into a voltage based on the detected resistance. The Lc's potential is held to 0V.

The E4990A device has 4 input channels from which it can perform analysis: Lcur, Lpot, Hcur and Hpot, which are analogous to the Lc, Lp, Hc and Hp mentioned previously. In order to have a negative bias for the analysis, the Hcur and Hpot terminals are connected to the cathode of the photodiode. Let's remember that in a photodiode the

Anode is always the terminal from which current flows into the device. By applying a positive potential to the cathode, we ensure a negative bias. The schematic for the CV measurements is shown in Figure 17.

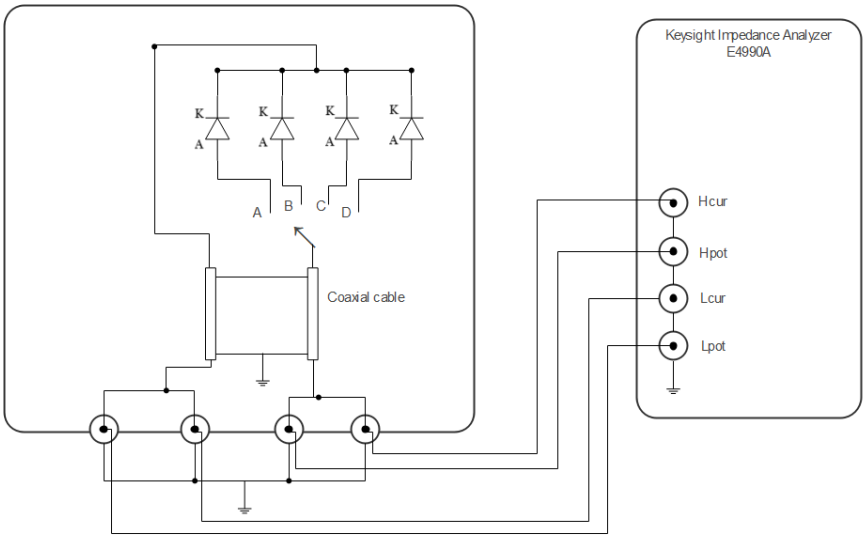

Figure 17: C-V measurement setup for the quadrant photodiodes.

As can be seen the quadrant of the photodiode of interest to analyze can be selected with a switch, while the cathode terminal remains fixed. Coaxial cables connect the E4990A to the measurement box, and inside the box coaxial cables are used to connect to the terminals of the photodiodes. Parasitic impedances can appear along the coaxial cables affecting the measurements, so a shielded 2T configuration is employed to minimize their effect. The shielded configuration is applied by connecting the shielding of the coaxial cables to the ground.

The E4990A device has two main ways to measure capacitance, by performing its own calculations depending on the equivalent circuit model considered for the Device Under Test (DUT). These two models are Cp and Cs, depending on if the model has a parallel parasitic resistance or a series parasitic resistance, as illustrated in Figure 18. Based on these equivalent circuit modes, calculations are done internally to provide the most accurate result. As we can remember from Figure 9, the equivalent circuit of a photodiode has both a series resistance R_S due to the cables and connections of the photodiode and a parallel shunt resistance R_{SH} which in an ideal photodiode is infinite. As the parallel shunt resistance is very large and the series resistance is almost negligible, the chosen equivalent circuit is the one with a parasitic parallel resistance, and therefore Cp will be the chosen output from the E4990A impedance analyzer.

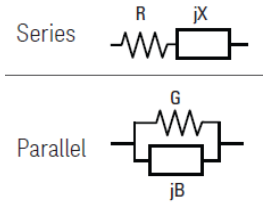

Figure 18: Equivalent circuit modes for the DUT in the E4990A device

There are multiple sources of parasitic impedance in the setup, caused by the internal resistance of the cables employed, the connections, parasitic capacitances in-between cables and layers of metal, as well as inductances. Methods exist to calibrate the setup using standardized resistances and components provided by the manufacturer, but they are only useful when using a test setup also provided by the manufacturer. Since our setup was developed in the Cleanroom of the OCA, such calibration methods are not optimal. Therefore, an open-short-load calibration method was selected for the calibration of the developed test fixture as it provided stable results across the frequency range of 20 Hz to 30 MHz.

As the name suggests, the open short load compensation is performed by doing an open circuit measurement, a short circuit measurement and a measurement with a load device for which the impedance values are well known. Once these measurements are done, measurements with the DUT are performed and the obtained values from the previous measurements are used in a formula that provides the corrected DUT impedance:

$$Z_{dut} = \frac{(Z_s - Z_{xm})(Z_{sm} - Z_o)}{(Z_{xm} - Z_o)(Z_s - Z_{sm}} Z_{std}$$

Where Z_{dut} is the corrected DUT impedance, Z_{xm} is the measured DUT impedance, Z_o is the measured open impedance, Z_s is the measured short impedance, Z_{sm} is the measured impedance of the load device and Z_{std} is the true value of the load device.

Several considerations must be considered when selecting a load device for the open-short-load compensation, such as using a stable resistor or capacitor as the load device, using a load of the same physical size and measure it in the same way as the DUT, use a load that is close in value to the DUT and use an accurately known load value. The author found that a 50 ohm resistor is the best possible load device to use as it provides the best results. Measurements with capacitors of different sizes and capacitance values as a load did not provide good results.

To test the ability of the setup to accurately measure capacitance over a wide range of frequencies, capacitors of different values were evaluated using the setup, and the results can be seen in Figure 19. On A it is possible to see the effect the parasitics have on the measurements when calibration is not performed properly, while on B the effect of proper calibration can be seen, keeping capacitance stable and accurate across all the frequency range.

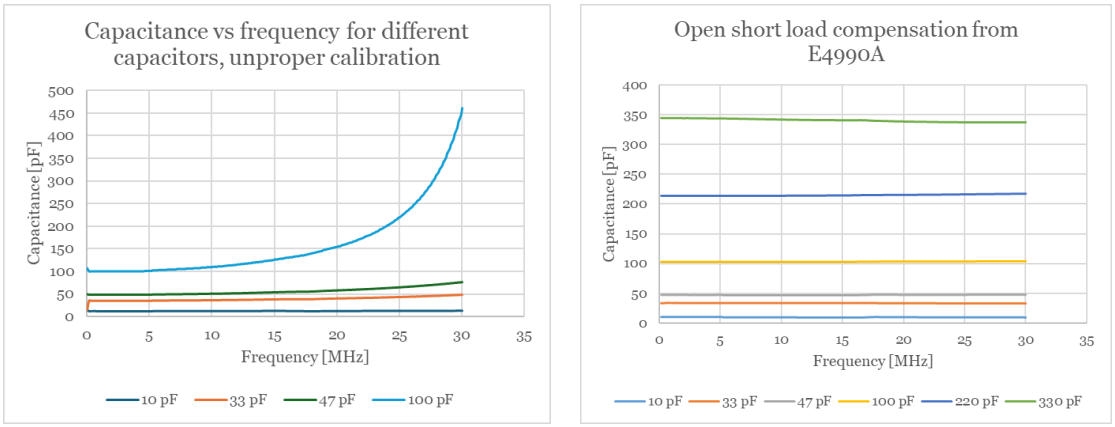

Figure 19: Capacitance vs Frequency for different capacitors. A) Unproper calibration results in incorrect capacitance measurement at high frequencies. B) Results with proper calibration and shielding

3.2.2 Current-Voltage (I-V) setup

The IV measurements were performed using the Keithley SMU 2635B device, alongside the Kickstart software to control it from a computer and perform voltage sweep and bias voltage measurements.

A special consideration must be considered when performing dark current measurements of quadrant photodiodes. As each quadrant acts individually as a photodiode, one could be tempted to only connect the anode of the quadrant of interest and the common cathode. However, the remaining quadrants, sharing the same cathode, suffer from its effects and contribute with leakage current to the measurements. To avoid this, the quadrants that are not being measured must have the anode connected to the ground. This way, whatever contribution to the leakage current they would provide, does not affect the measurement anymore. This can be seen in the schematic shown in Figure 20 used for the IV measurements:

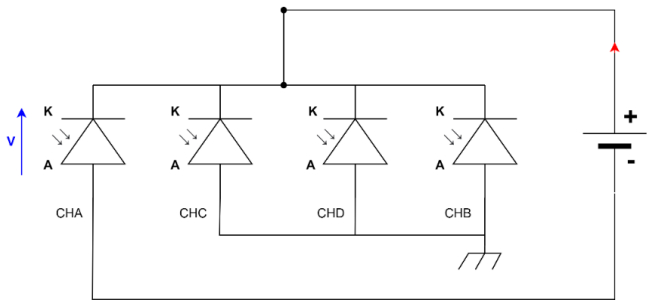

Figure 20: Quadrant photodiode proper bias for I-V measurements.

The problem of connecting the anode of each quadrant to either the measurement device or to the common ground was solved by implementing switches. Since the dark current depends on the temperature, a temperature sensor was also implemented into the setup, to better control the conditions of the photodiodes. The schematic showing the dark current measurement method can be seen in Figure 21.

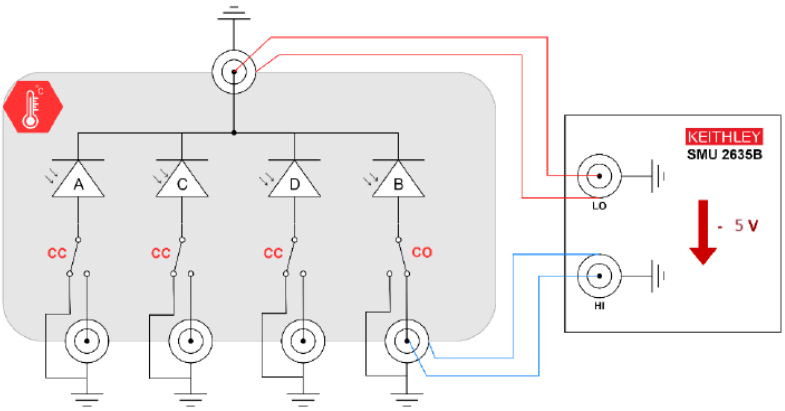

Figure 21: Quadrant photodiode dark current measurement schematic.

To ensure a temperature control during the measurements, a climatic chamber was used, and the temperature was monitored up to stabilization with the temperature sensor implemented inside the box and constant measurements taken by a MATLAB script. The temperature sensor is a Pt10K from Innovative Sensor Technology, Farnell. Based on the resistance obtained from the sensor, using Equation 3.1 the temperature can be calculated:

$$T[°C] = \frac{-A + \sqrt{A^2 - 4B\left(1 - \frac{R}{R_{T_0}}\right)}}{2B} \qquad 3.1$$

Where $A = 3.908 \times 10^{-3} °C^{-1}$, $B = -5.775 \times 10^{-7} °C^{-2}$ and $R_{T_0} = 10\ k\Omega$ at $T_0 = 0°C$. The MATLAB script does this calculation automatically and provides temperature measurements over time.

3.2.3 Combined I-V and C-V setup

The two measurement setups mentioned previously were put together into a single metallic box, without having one interfere with the other. To accomplish this, all connections from one setup were implemented on one side of the box, while the other setup was implemented on the other side of the box. In the end, two photodiode holders were located inside the box, one for IV measurements and the other for CV measurements, in a way that two measurements for two different photodiodes could be performed at the same time. The schematic of such a setup is illustrated in Figure 22. The same characteristics as for the CV and the IV setups were conserved, by allowing the connection of the anode to ground using a switch in the IV section and applying a shielding in the coaxial cables at the CV setup. This ensures that measurement is kept as similar as possible to both separated setups.

Not shown in the diagram is the temperature sensor Pt10K which is located in between the quadrant photodiodes inside the box. Both photodiodes are placed on fixtures soldered onto a perforated board to keep them fixed into place. The Pt10K sensor is also fixed to the perforated board by making use of kapton tape.

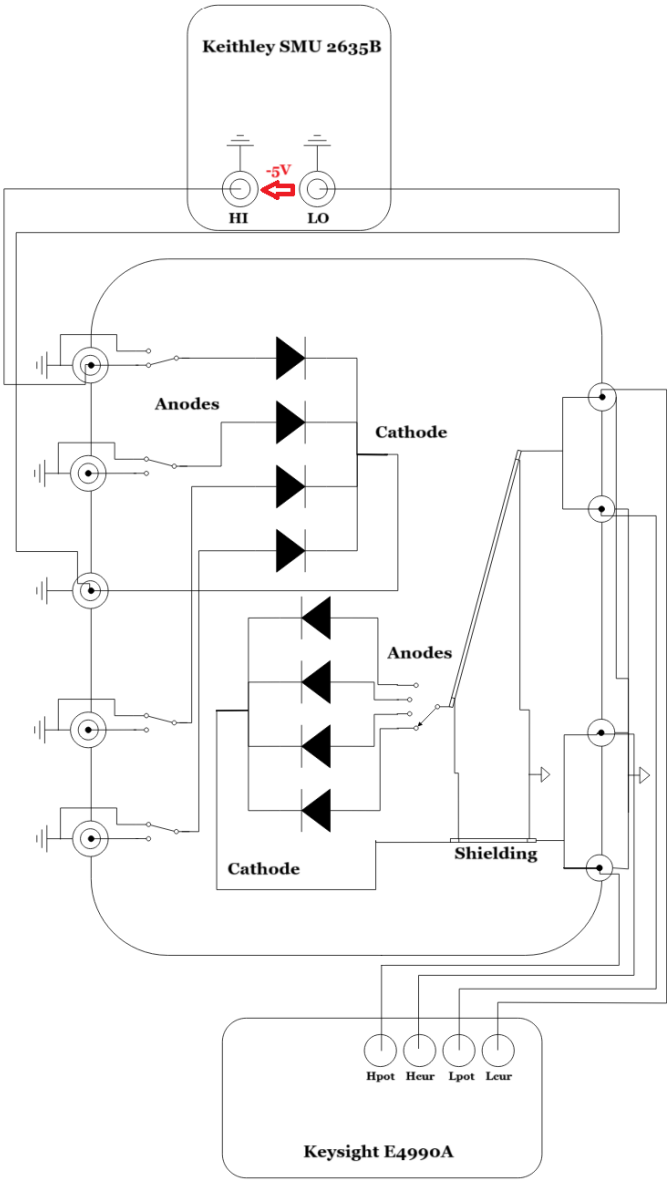

Figure 22: IV and CV setup diagram.

The physical implementation of both IV and CV combined in a setup is shown in Figure 23. On the left side we can see the IV connections which are, in descending order, A, B, Cathode, C and D, and they connect directly to the Keithley SMU 2635B. On the right side we can see the CV connections which are in descending order Hcur, Hpot, Lcur, Lpot, and they connect directly to the Keysight E4990A. On the middle, covered by an orange layer, we can see the Pt10K temperature sensor attached to the perforated board. Such a setup allows to take measurements of two photodiodes at the same time, measuring IV for one of them while measuring CV for the other. Since measurements have been performed at different temperatures using a climatic chamber, this arrangement allows to have minimum interference for both measurements at the same time, not affecting the temperature in-between one and other.

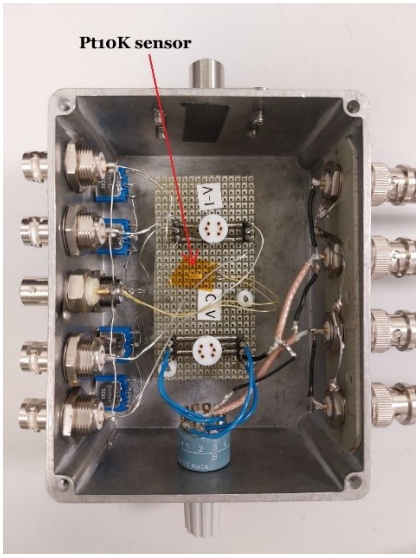

Figure 23: IV / CV setup physical implementation

The full measurement setup for the IV and CV measurements with temperature control is shown in Figure 24. On the sides of the climatic chamber there are apertures that can be sealed to prevent heat from escaping. Cables connecting the test box to the measurement instruments go through these apertures. To measure the CV characteristics of the photodiodes, the box is connected to the Keysight Impedance Amplifier E4990A. To measure IV characteristics, the box is connected to the Keithley 2635B and to keep temperature control, the Pt10K sensor in the test box is connected to the Hewlett Packard 34401A multimeter.

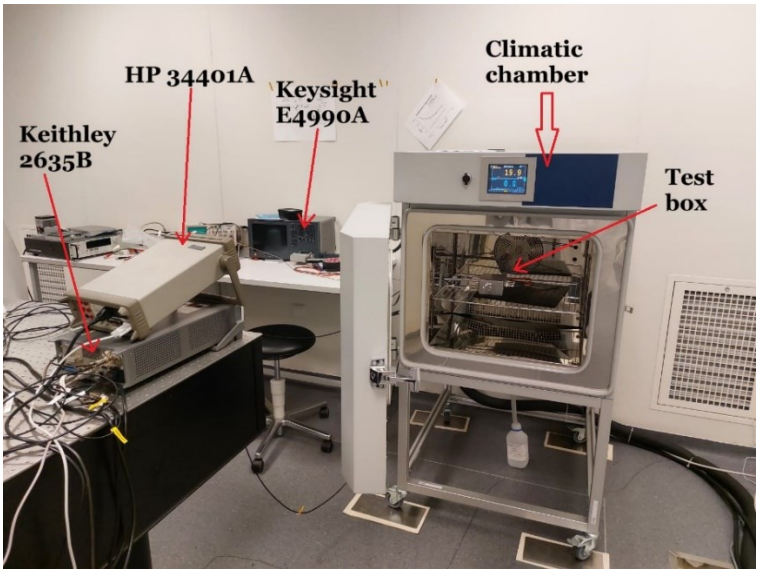

Figure 24: Full measurement setup for IV and CV measurements with temperature control

3.2.4 Setup Calibration

Before performing IV and CV tests on all photodiodes, first a good accuracy, good precision, and good repeatability must be ensured with the measurement setup. To ensure good precision, multiple measurements with the reference photodiodes (i.e. the non-irradiated photodiodes) were performed on 5 different days throughout the course of a week, connecting and disconnecting the photodiodes, turning on and off the measurement instruments, and ensuring a good temperature control of 20 °C by making use of the climatic chamber and waiting for temperature to stabilize. To keep extra control of the temperature, measurements were made every 10 seconds with the Pt10K temperature sensor inside of the measurement box. Such measurements were made with both the 1 mm reference photodiode and the 2 mm reference photodiode, taking IV sweeps from 0 to 5 V with 250 steps in-between. The mean value and the standard deviation of the IV sweeps at 5 V reverse bias of such measurements are shown in Table 3.5. The average temperature measured for each quadrant is also shown, to observe the variation between the temperature and the dark current measurements.

Table 3.5: IV precision measurements at 20 °C

QPD	**QPDJP 1 mm**				**QPDJP 2 mm**			
Segment	A	B	C	D	A	B	C	D
Mean [A]	1.19E-09	1.17E-09	1.11E-09	1.15E-09	2.55E-10	2.48E-10	2.64E-10	2.69E-10
Sdv [A]	4.59E-12	8.55E-12	6.83E-12	7.58E-12	8.79E-12	6.13E-12	4.60E-12	6.99E-12
Ratio (sdv/mean) (%)	0.387%	0.733%	0.614%	0.658%	3.454%	2.472%	1.745%	2.603%
Mean temperature [°C]	20.434	20.242	20.352	20.364	20.274	20.384	20.32	20.352
Sdv [°C]	1.79E-01	1.16E-01	1.55E-01	1.84E-01	2.46E-01	8.76E-02	0.00E+00	7.16E-02
Temperature ratio (sdv/mean) (%)	0.878%	0.574%	0.761%	0.901%	1.215%	0.430%	0.000%	0.352%

As can be seen, the standard deviation- mean ratio is less than 1% for the 1 mm reference photodiode, while it reaches up to 3.4% for the 2 mm reference photodiode, indicating that there is good precision in the measurements and therefore good repeatability. The ratio between standard deviation and the mean value for the temperature reaches values below 1%, except for quadrant A for the 2 mm photodiode, where also a higher variation for the dark current can be seen.

Following the same procedure of taking 5 measurements on different days, disconnecting and connecting, turning on and off instruments and keeping a temperature control of 20 °C, CV measurements were also made, by applying frequency sweeps from 20 Hz to 30 MHz at reverse bias voltages ranging from 0 to 5 V. Table 3.6 shows the mean value and standard deviation of CV measurements at 10 MHz and at a reverse bias of 5 V, for the 1 mm and 2 mm reference photodiodes.

Table 3.6: CV precision measurements at 20 °C.

QPD	**QPDJP 1 mm**				**QPDJP 2 mm**			
Segment	A	B	C	D	A	B	C	D
Mean [F]	6.23E-12	6.52E-12	6.83E-12	6.64E-12	1.48E-11	1.51E-11	1.58E-11	1.55E-11

Sdv [F]	2.43E-14	5.21E-14	7.98E-14	9.57E-14	1.28E-14	1.11E-14	5.84E-15	7.10E-15
Ratio (sdv/mean) (%)	0.390%	0.799%	1.170%	1.440%	0.087%	0.074%	0.037%	0.046%

The standard deviation-mean ratio is 1.44% at the highest value for the 1 mm reference photodiode, while it is less than 0.1% for the 2 mm reference photodiode, once again ensuring good precision and repeatability in the measurement setup. As temperature has an effect of less than 50 femtofarads for the capacitance, the variation for temperature measurements are not shown on Table 3.6.

To evaluate the accuracy of the setup, it was decided to compare its performances with the ones of the setup located at ONERA. This way, taking the values measured at OCA as the observed values and taking the values measured at ONERA as the real values, it would be possible to obtain a measure of the accuracy at different temperatures for the 3 different photodiode sizes, comparing the reference photodiode values. The accuracy can be seen for the mean of the 4 quadrants, for each size's reference photodiode, for the IV measurement in Table 3.7.

Table 3.7: Accuracy of the IV setup comparing OCA and ONERA measurements

Accuracy at 20 ° C			
QPD	QPDJP 1 mm	QPDJP 1.5 mm	QPDJP 2 mm
OCA values	1.15069E-09	2.13174E-10	2.58823E-10
ONERA values 2022/10/11	1.12227E-09	2.06506E-10	2.47581E-10
Accuracy	97%	97%	94%
Accuracy at 30 ° C			
QPD	QPDJP 1 mm	QPDJP 1.5 mm	QPDJP 2 mm
OCA values	2.11125E-09	5.00538E-10	
ONERA values 2022/10/11	2.06202E-09	4.65369E-10	
Accuracy	98%	92%	
Accuracy at 35 ° C			
QPD	QPDJP 1 mm	QPDJP 1.5 mm	QPDJP 2 mm
OCA values			9.87862E-10
ONERA values 2022/10/11			9.11778E-10
Accuracy			92%
Accuracy at 40 ° C			
QPD	QPDJP 1 mm	QPDJP 1.5 mm	QPDJP 2 mm
OCA values	3.85056E-09	1.20E-09	
ONERA values 2022/10/11	3.74018E-09	1.10572E-09	
Accuracy	97%	92%	
Accuracy at 50 ° C			
QPD	QPDJP 1 mm	QPDJP 1.5 mm	QPDJP 2 mm
OCA values	6.70771E-09	2.77889E-09	3.58704E-09
ONERA values 2022/10/11	6.65383E-09	2.55858E-09	3.44131E-09
Accuracy	99%	91%	96%

As can be seen, an accuracy above 97% is seen for the 1 mm photodiodes across all temperatures. For the 1.5 mm and the 2 mm photodiodes, at 20 °C the accuracy can have a discrepancy of up to 6%, which increases as the temperature increases to a maximum of 9%. Such accuracies obtained are considered for the IV measurements of the rest of the tested photodiodes. The comparison between measurements done at OCA and at ONERA for the reference photodiodes is shown in Figure 25. The solid lines are the mean value between the quadrants, the grey zone is the standard deviation across the quadrants and the error bar is the accuracy.

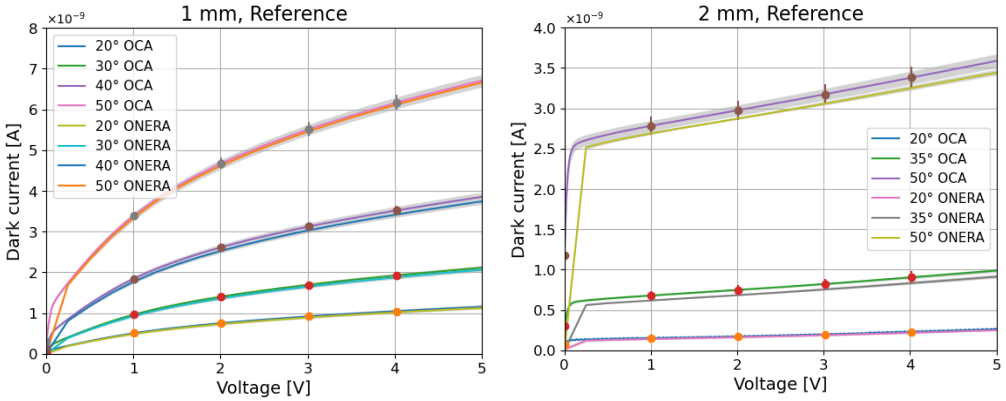

A) 1 mm B) 2 mm

Figure 25: OCA and ONERA Reference photodiodes IV measurement comparison

Regarding the CV accuracy, it was discovered after some analysis that the data captured at ONERA had considerable variations depending on when the measurements were performed. This can be seen in Figure 26 where data taken on different dates at ONERA gives a variation of 1 pF for the 1 mm photodiode, 2 pF for the 1.5 mm photodiode and 3.5 pF for the 2 mm photodiode. The plotted line is the mean value of the 4 quadrants while the grey zone is the standard deviation between them.

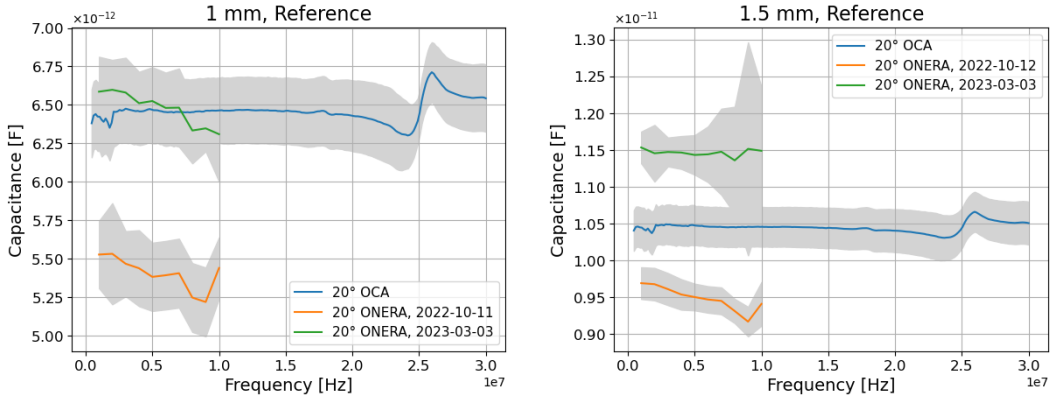

A) 1 mm B) 1.5 mm

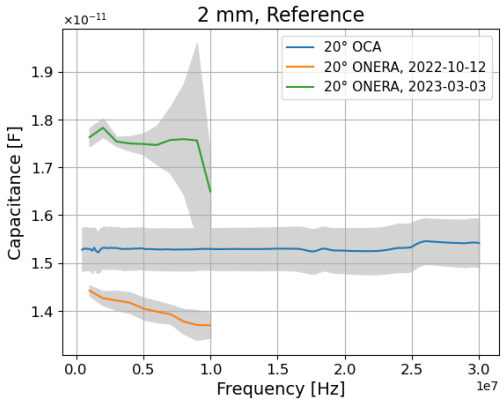

C) 2 mm

Figure 26: CV measurements for reference photodiodes

Because of these variations, data obtained at OCA was the only one taken as reference for the CV measurements performed with the irradiated photodiodes.

3.3 Tests conditions

To measure the irradiated photodiodes, the same procedure was followed as the one to measure the reference photodiodes for the calibration of the measurement setup. The measurement box was located inside the climatic chamber and connected to the Keysight Impedance Analyzer E4990A for the capacitance measurements, the Keithley SMU 2635B for the dark current measurements and the HP34401A for the temperature measurements along with the Pt10K sensor. Photodiodes were put inside the box connected to the test fixtures, one for the capacitance fixture and another one for the dark current fixture. The climatic chamber was sealed, and the target temperature was set up. The time for the temperature stabilization inside the box (monitored with the Pt10K sensor) was around 50 minutes, and then IV sweeps from 0 to 5 V with 250 steps in-between were taken, as well as capacitance frequency sweeps from 20 Hz to 30 MHz with a 5 V bias, for each channel, for each photodiode, for each temperature (20, 35 and 50°C).

4. Results and analysis

After performing CV and IV measurements for the reference and irradiated photodiodes, data acquired from the systems was extracted and analyzed using python scripts. Such data was then plotted for a better understanding of the effects occurring after irradiation on the photodiodes.

4.1 Dark current

Dark current measurements acquired from the Kickstart software controlling the Keithley SMU 2635B were analyzed and data obtained was plotted for each of the irradiation conditions, for each of the photodiode sizes. The dark current for the proton, electron and gamma irradiated photodiodes will now be presented.

4.1.1 Proton irradiated photodiodes

On Figure 27 it is possible to see the dark current results for the 20 MeV proton irradiated photodiodes. Dark current at three different temperatures (20, 35 and 50°C) can be seen on each plot of the figure. Pre-irradiation and post-irradiation dark current measurements performed at ONERA are displayed, along with the measurements performed at OCA with the developed setup. The plotted line is the mean value over the 4 quadrants of each photodiode, and on grey, the standard deviation of the four quadrants is indicated. Error bars associated to the accuracy corresponding to the difference between the reference photodiodes' measurements is indicated with a circle with lines extending on the y-axis.

For the 1 mm photodiodes, shown in Figure 27 A, Dark current can go as high as 1.33 µA at 50°C, 484 nA at 35°C and 164 nA at 20°C after proton irradiation when reaching a 5 V reverse bias, while pre-irradiation measurements have values of 6.7 nA at 50°C, which remains negligible compared to all the post-irradiation measurements. The 1.5 mm photodiodes shown in Figure 27 B show a similar behavior, in which the pre irradiation measurement has a value of 3 nA at 50°C while post irradiation measurements show a dark current of 320 nA at 20°C, 953 nA at 35°C and 2.6 µA at 50°C and 5 V reverse bias. Lastly, the 2 mm photodiodes, which once again show a similar behavior, have a pre irradiation dark current of 4 nA at 50°C, and a post irradiation dark current of 520 nA at 20°C, 1.6 µA at 35°C and 4.4 µA at 50°C.

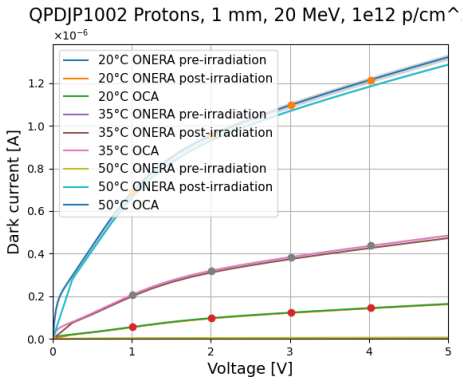

A)

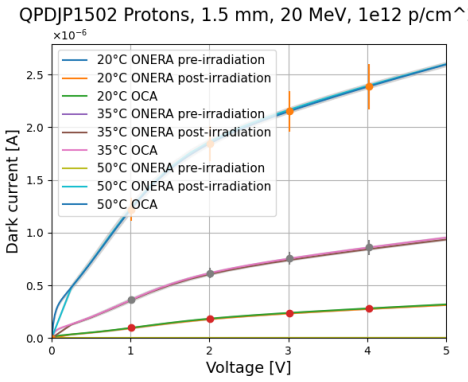

B)

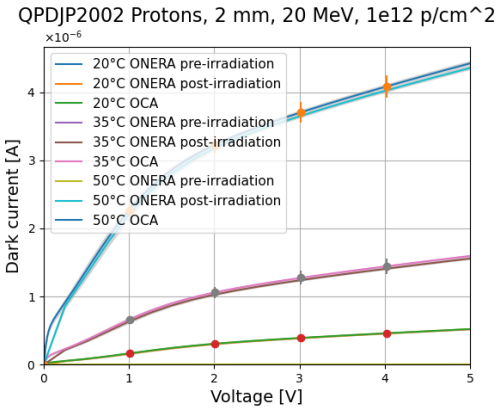

C)

Figure 27:Dark current for the 20 MeV Proton irradiated photodiodes.

As can be seen, the post irradiation measurements performed at ONERA provide values within the error bars of the measurements performed at OCA, indicating that the dark current measured was the same in both setups. A difference in time of over 500 days did not affect the observed dark current, indicating that there were no annealing phenomena taking place during this time. It is important to mention that dark current measurements performed at ONERA for the proton irradiation were done after more than 24 hours of the irradiation. A possible explanation of the measured results is that proton irradiation mainly causes ionization and displacement damage in a crystal lattice. Due to the interaction type which might be elastic (displacement damage) or non-elastic (nuclear reactions), it is possible that the annealing after one year did not influence the displacement damage or the nuclear reactions which could create damage clusters in the crystal lattice. There was a high number of nuclear reactions (5.77×10^6) calculated using Equation 4.1 using cross section values evaluated using software Geant4, for a fluence of $1 \times 10^{12} cm^{-2}$[36].

$$n = S \cdot W \cdot \sigma \cdot \Phi \cdot N \qquad 4.1$$

Where n is the number of nuclear reactions, S is the surface area of the photodiode, W is the depletion region width, Φ is the fluence, N the number of atoms per cm^{-3} and σ is the nuclear cross section. Such a high number of nuclear reactions might explain the fact that no annealing effect can be observed after more than 1 year of irradiation, as recombination of defects caused by them might require proper annealing at higher temperatures.

Also, since the dark current increases so much at high temperatures, EFE might be playing a very important role as carrier thermal generation could explain the difference between the pre irradiation and the post irradiation measurements. As we are working with a reverse bias saturation electric field of 5 V, defective clusters play a more important role in the carrier generation than point defects [32].

As for the ionization damage, annealing of this phenomenon is possible to have taken place right after irradiation, in the 24 hours between irradiation and dark current measurements with the ONERA setup, leaving no observable ionization damage annealing after this period.

Similar behavior can be observed for the photodiodes irradiated with protons at 60 MeV in Figure 28. A discrepancy observed at 50°C for the 1 and 1.5 mm photodiodes and at 35°C and 50°C for the 2 mm photodiodes was due to instrumental error, as the measurement setup was moved from ONERA to the irradiation location. Nevertheless, at all other temperatures it is possible to observe that the post irradiation dark current measurements done with the ONERA setup give values within the error bars of the measurements performed at OCA, indicating that there is no annealing effect between measurements regardless of the amount of time between them.

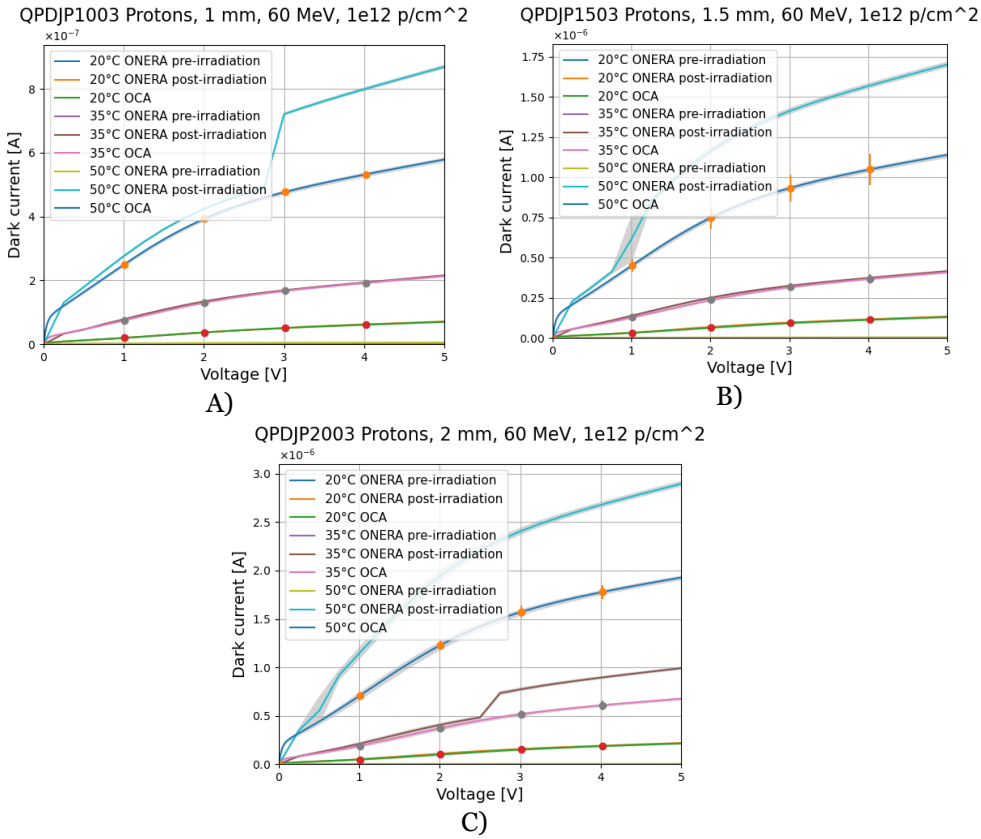

Figure 28: Dark current for the 60 MeV Proton irradiated photodiodes.

For the 1 mm photodiode irradiated with 60 MeV protons, a pre irradiation dark current of 5.8 nA was measured at 50°C while post irradiation values were 70 nA at 20°C, 213 nA at 35°C and 580 nA at 50°C, all at a reverse bias voltage of 5 V. In the case of the 1.5 mm photodiode, a dark current of 3.96 nA at 50°C and 5 V reverse bias voltage was observed, while the post irradiation dark currents were 130 nA at 20°C, 410 nA at 35°C and 1.14 µA at 50°C also at 5 V reverse bias voltage. Lastly, the 2 mm photodiode had a pre irradiation dark current of 4 nA at 20°C while the post irradiation dark currents were 213 nA at 20°C, 6.76 nA at 35°C and 1.93 µA at 50°C.

It is interesting to notice how the 20 MeV proton irradiation causes a higher dark current than the 60 MeV proton irradiation for all photodiodes, by almost a factor of 2. A possible explanation is that at lower proton energies, the Bragg peak is reached at a lower depth and thus more defect clusters appear in the depletion region of the photodiodes, while higher energy protons go through the device without reaching this stopping power peak, causing less overall damage. It has been reported that for 150 keV proton irradiation in InGaAs, the Bragg peak is located within a 1.7 µm target depth

[38], and although there is a big difference in energy between 150 keV and 20 MeV, this might explain how being closer to the Bragg peak plays a big role in creating more defects within the crystal lattice.

Such a phenomenon is better explained in 57Figure 29 where Monte Carlo SRIM [39] simulations were run for protons with their respective energies (20 MeV on A and 60 MeV on B), assuming a depth of 300 μm of InGaAs and a number of 10000 incident particles. For these basic simulations, the number of vacancies generated per ion was 10.4 in the case of the 20 MeV protons while it was 3.1 for the case of the 60 MeV protons. Such numbers should not be taken accurately into account as the details of the used technologies are unknown, but they serve for qualitative assessment into understanding the increase in dark current having protons with less energy.

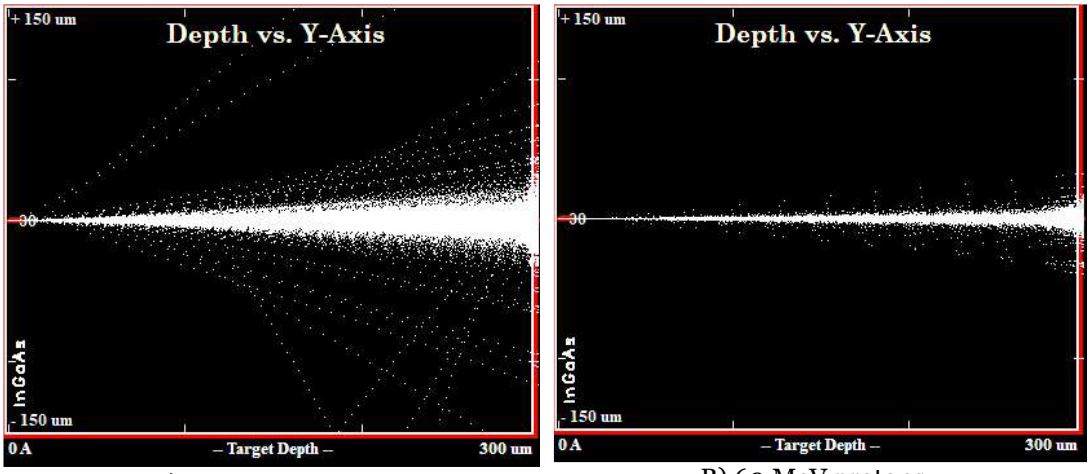

A) 20 MeV protons B) 60 MeV protons

57Figure 29: SRIM simulations for 20 and 60 MeV protons on InGaAs.

4.1.2 Electron irradiated photodiodes

The Dark current measurement results for the electron irradiated LISA Mission photodiodes are shown in Figures 30 and 31. Pre irradiation measurements performed at ONERA, post irradiation measurements performed at ONERA and post irradiation measurements performed at OCA are observed for each subplot, at three different measurements: 20, 35 and 50°C.

Figure 30 shows the 0.5 MeV electron irradiated photodiodes. Post irradiation dark current measurements with the setup from ONERA took place right after irradiation, and is shown in orange for each subplot, while pre irradiation measurements are shown with a blue line and the dark current measured at OCA is observed in green. The solid lines indicate the mean value between the quadrants of the photodiode, while the grey shaded area represents the standard deviation between the channels, and an error bar indicating the accuracy between measurements done at OCA and at ONERA is applied on top of the OCA lines. For each measurement done at OCA, the number of days after irradiation is indicated, to better understand the difference between the post irradiation measurements done at ONERA and at OCA. As can be seen, the post irradiation dark currents have a discrepancy that goes beyond the error bars, indicating a true difference

in the dark current which indicates that throughout this period, annealing took place in the device.

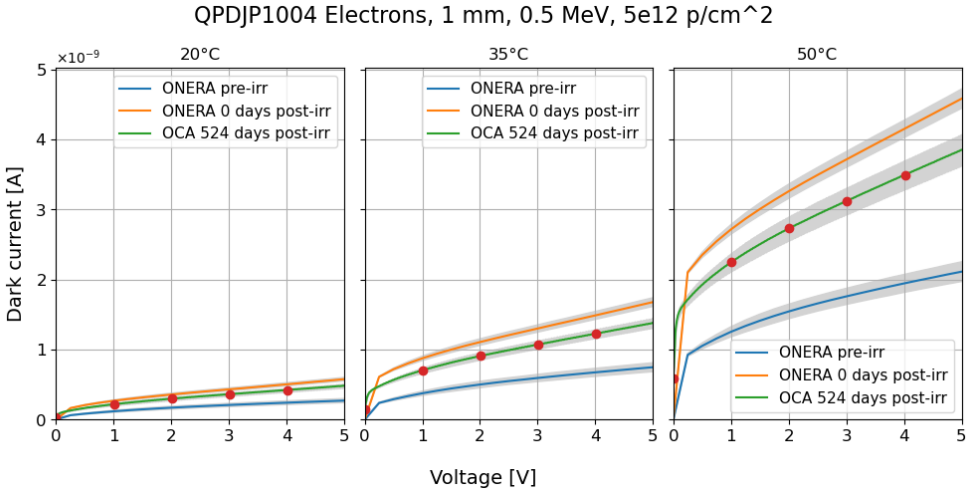

A)

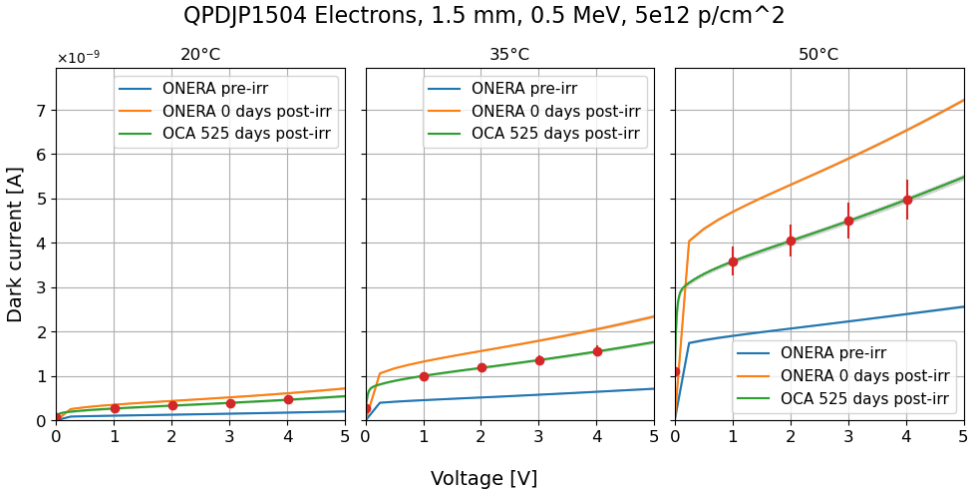

B)

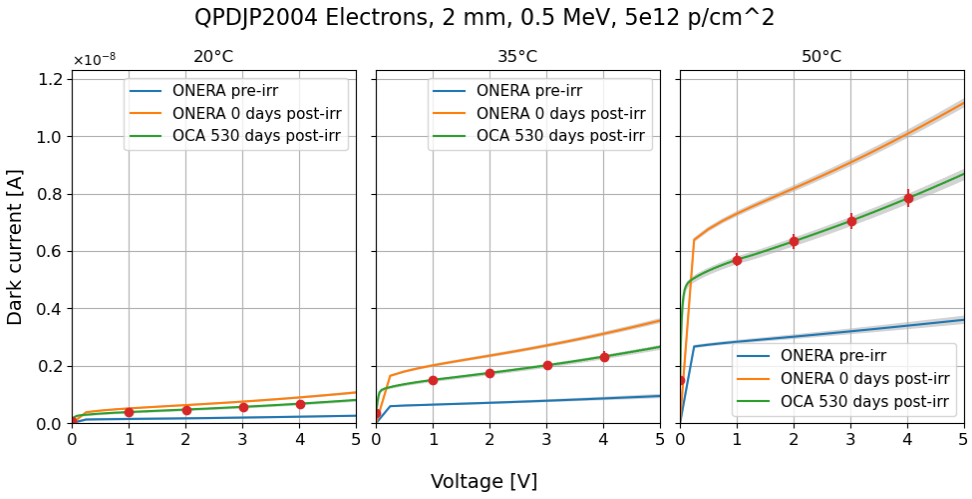

C)

Figure 30: Dark current for the 0.5 MeV Electron irradiated photodiodes.

In Figure 30 A, for the 0.5 MeV electron irradiated 1 mm photodiode, ONERA post irradiation dark current measurements have a value of 5.045 nA at 50°C while the OCA measurements at the same temperature have a value of 3.91 nA also at 50°C, and the pre irradiation measurements at 50°C provide a value of 2.3 nA at 50°C. The ratio of decrease of the dark current between the ONERA measurement and the OCA measurement with respect to the pre irradiation measurement is 41.35%. A similar behavior can be observed at temperatures of 35°C and 20°C.

In Figure 30 B for the 1.5 mm 0.5 MeV electron irradiated photodiode, pre irradiation, ONERA post irradiation and OCA post irradiation dark current measurements at 50°C are shown. Their values are 2.7 nA, 7.96 nA and 5.5 nA, respectively. The ratio of decrease of the dark current between the ONERA measurement and the OCA measurement with respect to the pre irradiation measurement is 46.77%, which is close to the ratio observed for the 1 mm photodiode. Again, the same behavior is seen in the plots corresponding to the 20°C and 35°C measurements.

In the case of Figure 30 C for the 2 mm 0.5 MeV electron irradiated photodiode, pre irradiation, ONERA post irradiation and OCA post irradiation dark current measurements are shown also at 50°C. Their values are 3.76 nA, 12.2 nA and 8.68 nA, respectively. The ratio of decrease of the dark current between the ONERA measurement and the OCA measurement with respect to the pre irradiation measurement is 41.7%, which is like the ratio observed for the 1 mm and 1.5 mm photodiodes.

Electrons can have elastic collisions with atoms in which they cause displacement damage, but they can also have inelastic collisions in which there might be excitation of energy levels of electrons from target atoms or ionization. Out of these interactions, the most dominant is ionization damage. It is possible that this ionization damage was not as stable and permanent as the damage caused by 20 and 60 MeV protons, and therefore annealing took place throughout the period over 500 days after irradiation. The ionization caused by the shower of particles generated by an incident electron (having pair production generation, Compton scattering, Bremsstrahlung emission, etc.) was able to have recombination within the lattice during that period.

Figure 31 shows the dark current measurements for the 1 mm and 2 mm photodiodes irradiated with 1 MeV electrons. There was no 1 MeV electron irradiation for the 1.5 mm photodiode since the number of photodiodes was limited and it was chosen for the Gamma ray irradiation. Just as for the 0.5 MeV electron irradiated photodiodes, the post irradiation measurements taken at ONERA indicate a higher dark current than the measurements taken at OCA, going beyond the error bars, indicating annealing took place for the photodiodes. Following a similar procedure as for the 0.5 MeV electron irradiation, the ratio of decrease of the dark current between the ONERA measurement and the OCA measurement with respect to the pre irradiation measurement at 5 V reverse bias and 50°C is 38.52% for the 1 mm photodiode, while it is 38.68% for the 2 mm photodiode, and the same behavior is seen also at 20°C and 35°C.

Although electrons don't exhibit the same stopping power behavior as protons, a higher deposited energy for incident electrons with lower energies has been reported for electrons interacting with H, He and H_2 [40]. Therefore, it can be expected that also higher energies are deposited by lower energy electrons on InGaAs, expecting variations depending on the cross section.

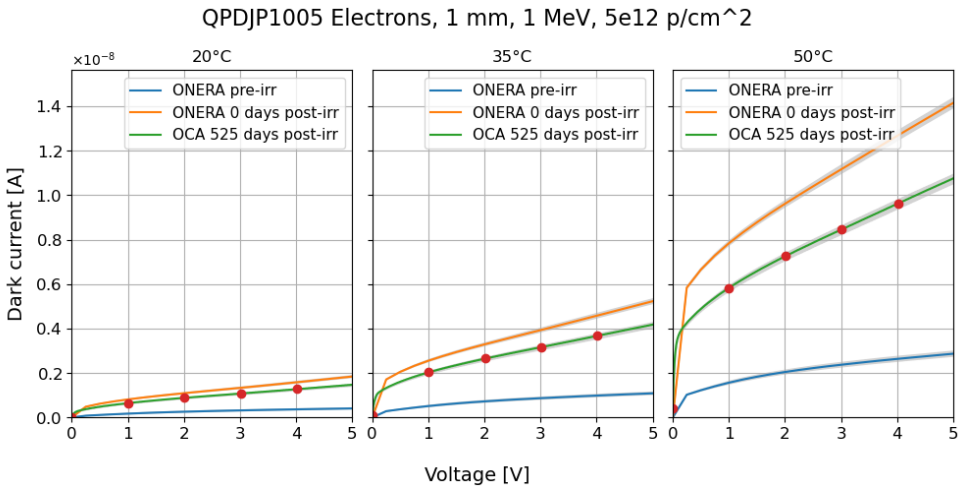

A)

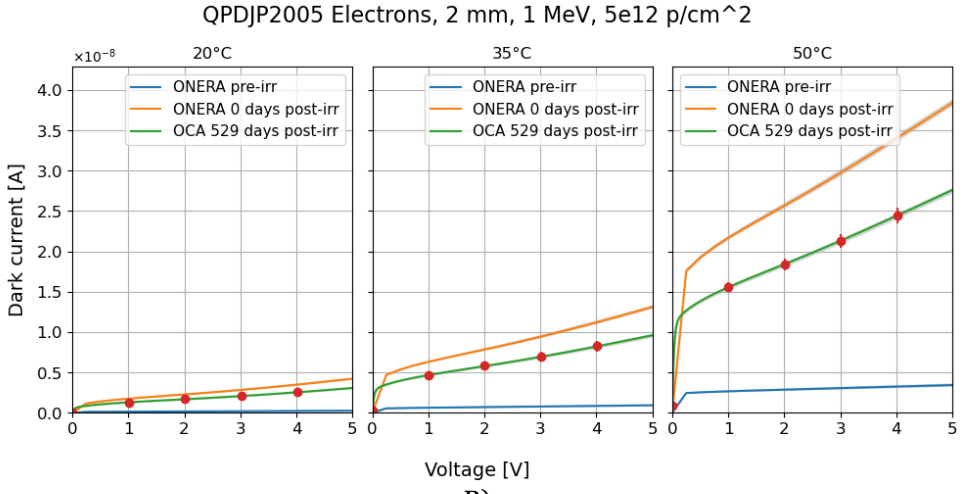

B)

Figure 31: Dark current for the 1 MeV Electron irradiated photodiodes.

Although more than 60% increase of the dark current is still observed, which as explained in 2.2.2, could be due to the production of a defect level in the band gap, which was denoted E2, located 0.29 eV below the fermi level (i.e. Ec-E2 = 0.29 eV) which act as a generation center in the photodiode.

4.1.3 Gamma-rays irradiated photodiode

The Dark current measurement results for the Gamma ray irradiated quadrant photodiode are shown in Figure 32. For this photodiode, a particular post-annealing process of 3 steps was followed. On the first step, the device was set at 96 hours at room temperature and no bias voltage. On the second step, the device was set for 24 hours at room temperature with a reverse bias of 5 V, and on the third step, the device was set for 168 hours at 100°C and 5 V reverse bias. Post annealing dark current measurements are shown in the plots, in addition to the pre irradiation measurements performed at ONERA, post irradiation measurements performed at ONERA, and post irradiation measurements performed at OCA, at three different temperatures: 20, 35 and 50°C.

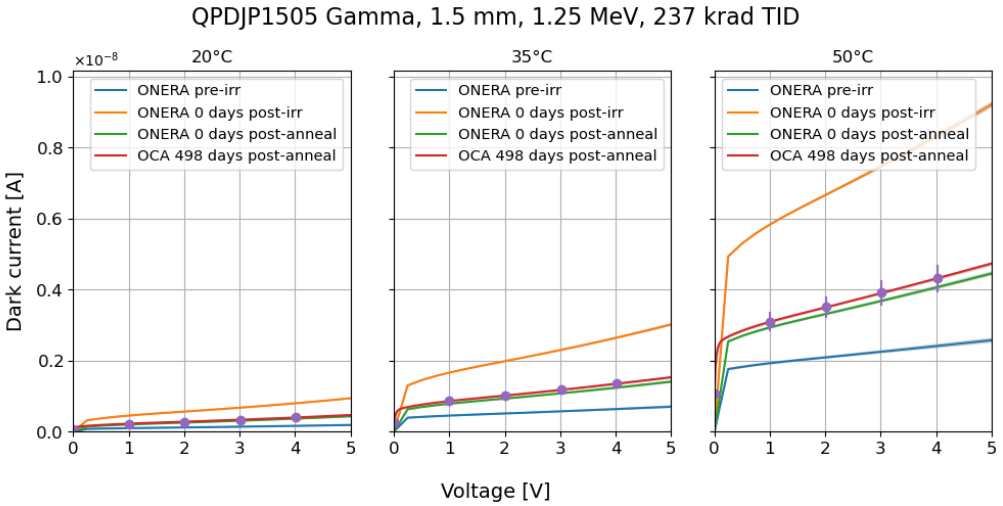

Figure 32: Dark current for the Gamma-ray irradiated photodiode.

As can be seen, there is no post annealing effect after 498 days as the measurements fall within the error bars, indicating that the same dark current value was measured right after annealing in ONERA and at OCA.

4.2 Capacitance

C-V frequency sweeps from 20 Hz to 30 MHz were applied to the reference and irradiated photodiodes, for each photodiode size, and the results are shown in Figures 33, 34 and 35. Each plot contains, for each photodiode size, the reference (non-irradiated) as well as each irradiated photodiode for that size.

Figure 33 shows the capacitance measurements for the 1 mm photodiodes. As can be seen the approximate capacitance value is 6.6 pF, with slight variations depending on the type of irradiation. On grey it is possible to see the standard deviation of the 4 quadrants for each photodiode, while the solid line represents the mean value over the 4 quadrants. Error bars indicate the precision obtained for the CV measurements for the reference photodiodes.

It is possible to see that the reference photodiode has a slightly lower capacitance than the rest of the irradiated photodiodes, being the proton irradiated photodiodes the ones with the highest capacitance values. Although the difference is around 0.28 pF across all frequencies, indicating that the change in capacitance is very low. It is also between the standard deviation of the photodiodes' quadrants, making conclusions unclear regarding the radiation effect on the capacitance.

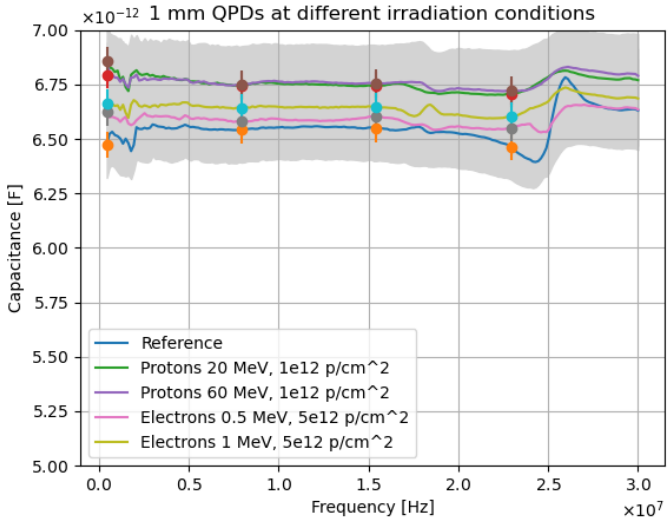

Figure 33:Capacitance for the 1 mm photodiodes at different irradiation conditions

Figure 34 shows the CV frequency sweeps for the 1.5 mm photodiodes, irradiated and non-irradiated. A similar behavior as for the 1 mm photodiodes can be observed, in which there is a higher capacitance for electron irradiated photodiodes and for proton irradiated photodiodes, being the biggest difference between the reference photodiodes and the proton irradiated photodiodes of around 0.56 pF across all frequencies. It is interesting to notice how the capacitance of the electron irradiated photodiodes is in-between that of the proton irradiated and the reference photodiodes, indicating that there is a greater effect on capacitance caused by proton irradiation as compared to electron irradiation. Nevertheless, the variation is so small (less than 1 pF) and within the standard deviation of the measurements, that no accurate conclusion can be drawn from these results.

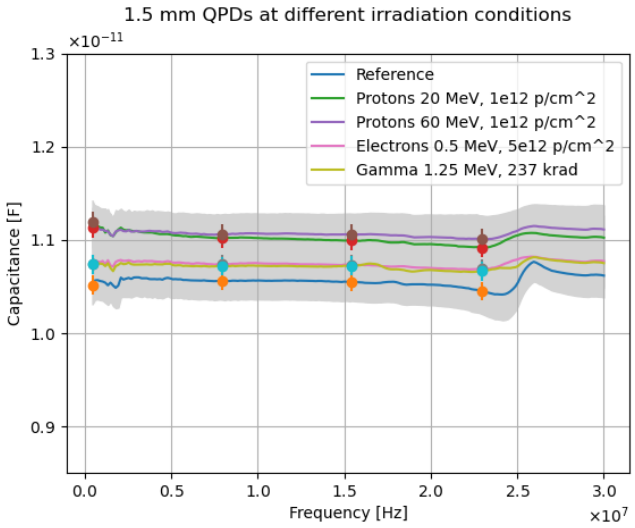

Figure 34:Capacitance for the 1.5 mm photodiodes at different irradiation conditions

Figure 35 shows the capacitance frequency sweeps for the 2 mm photodiodes at different irradiation conditions. Compared to the results observed on the 1 mm and 1.5 mm photodiodes, the effect of 60 MeV proton and 1 MeV proton irradiations did not change the capacitance as compared to the reference photodiode, while the 20 MeV proton irradiation has a capacitance difference of 0.73 pF as compared to the reference, which goes beyond the standard deviation of the reference photodiode but is still an inconclusive result as the variation is less than 1 pF and one cannot tell the distinction between the standard deviations of the photodiodes. The case of the 0.5 MeV electron irradiated photodiode is particular as one of the quadrants reaches breakdown at 1.1 V reverse bias voltage, which might play a role in the capacitance observed at the other channels within the photodiode. Still, variation is so low that once again can be considered negligible, and radiation has no significant effect on the capacitance of the photodiodes.

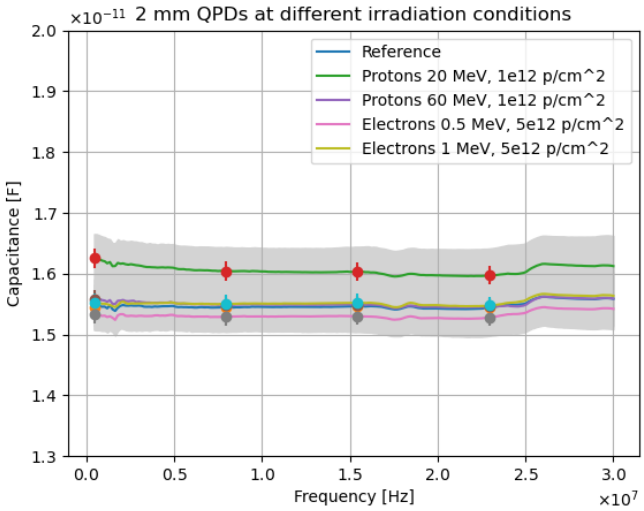

Figure 35:Capacitance for the 2 mm photodiodes at different irradiation conditions

An explanation to the increase in capacitance observed by irradiation could be that there is an introduction of donor and acceptor levels, which was already discussed for the case of electrons, below the Fermi level, enhancing carrier concentration, which might make the depletion region thinner, increasing capacitance as the distance between the p and n type semiconductors would be shorter.

4.3 Non-Ionizing Energy Loss

As previously mentioned in 2.2, the NIEL scaling approach is a method to scale the expected device degradation from one radiation type to another, from one applied energy to another. It serves as a basis for limited irradiation campaigns, since from the device response to a particular radiation type and energy, the NIEL response can be predicted for radiation at other energies. A screened relativistic (SR) treatment for NIEL dose nuclear and electronic stopping power calculator can be found at [41]. This method is based on the screened relativistic treatment for Coulomb interactions on nuclei from low to ultra relativistic energies. By making use of damage factors obtained from the experimental data, it is possible to apply the NIEL scaling approach.

4.3.1 Damage factors

Damage factors represent how much degradation of one parameter is caused by a single incident particle in a crystal semiconductor lattice. They can be calculated directly from experimental data, by using the universal damage factor formula [42] (modified due to the fact of the indeterminate width of the depletion region) shown in Equation 4.2.

$$K_{dark} = \frac{I_{dark}(\Phi) - I_{dark}(0)}{\Phi \cdot A} \qquad 4.2$$

Where K_{dark} is the damage factor, $I_{dark}(\Phi)$ is the dark current after irradiation, $I_{dark}(0)$ is the dark current before irradiation, Φ is the applied fluence and A is the surface area of the photodiode.

Following the photodiode assigned numbers from Table 3.4, the damage factors for proton irradiation is shown in Figure 36. Error bars for damage factors indicate propagation of error including accuracy and standard deviation using the min-max method [43].

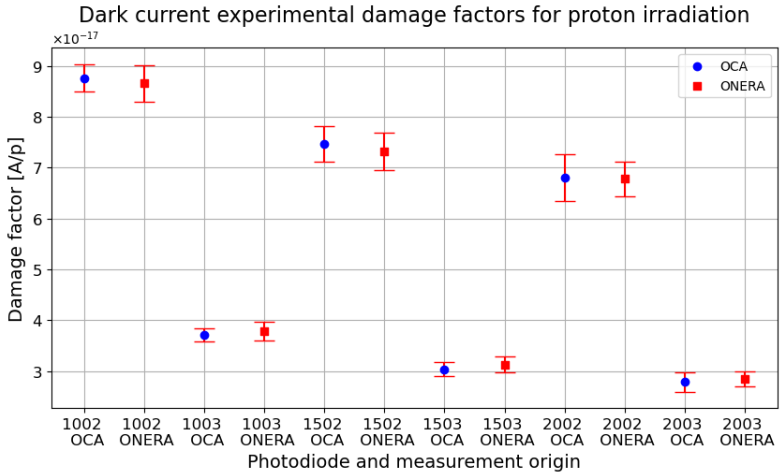

Figure 36: Photodiode damage factors for proton irradiation at 20 MeV (ending in 2) and at 60 MeV (ending in 3), for 1 mm, 1.5 mm and 2 mm diameters (starting with 10, 15 and 20 respectively).

Damage factors from measurements performed at both OCA and ONERA provide values that fit within the error bars of each other, indicating again that there was no annealing from proton irradiation as discussed earlier. An interesting trend is observed in which the damage factors decrease along with the diameter of the photodiodes. 20 MeV proton irradiation provides a higher damage factor than 20 MeV proton irradiation.

Figure 37 shows the damage factors obtained from electron irradiation on the photodiodes, once again the x axis shows the number assigned to each photodiode based on its diameter and the irradiation type and energy based on Table 3.4. A lower damage factor is observed from the measurements performed at OCA, once again indicating annealing took place during the time between the ONERA measurements and the OCA measurements. The same trend of having a lower damage factor as the photodiode diameter increases is observed, as for the proton irradiation.

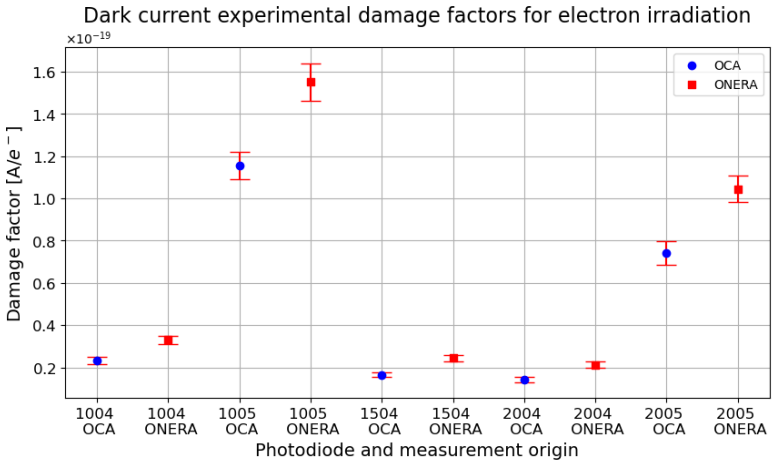

Figure 37: Photodiode damage factors for electron irradiation at 0.5 MeV (ending in 4) and at 1 MeV (ending in 5), for 1 mm, 1.5 mm and 2 mm diameters (starting with 10, 15 and 20 respectively).

4.3.2 NIEL scaling approach applied to Dark current

Using values obtained for the damage factors, NIEL scaling approach can be applied by using Equation 2.1:

$$NIEL = K_{dark} \cdot \frac{NIEL(p^+, 20\ MeV)}{K_{dark}(p^+, 20\ MeV)} \qquad 4.3$$

Where $NIEL$ is the Non-Ionizing Energy Loss in $MeV/g \cdot cm^2$ for a particular K_{dark}, which is the damage factor for a particular photodiode, for a particular irradiation condition. $K_{dark}(p^+, 20\ \text{MeV})$ is the damage factor for proton irradiation at 20 MeV and $NIEL(p^+, 20\ \text{MeV})$ is the NIEL for proton irradiation at 20 MeV, obtained from simulations by making use of the SR NIEL calculation tool. Displacement threshold energies applied by default by the calculator are 43 eV for In, 21.5 eV for Ga and 21.5 eV for As.

For this work, the damage factor of the 20 MeV proton irradiated 1 mm diameter photodiode was used to obtain the scaling factor, which was then further applied to other energies and irradiation types. Using the same scaling factor for the 1.5 mm and 2 mm, for both proton and electron irradiation, NIEL values were obtained and compared to NIEL curves obtained from the SR NIEL calculator.

Figure 38 shows the NIEL scaling approach applied to the proton irradiated photodiodes, considering measurements both done at ONERA and at OCA. On red, the NIEL curve for proton irradiation on $In_{0.53}Ga_{0.47}As$ obtained from the SR NIEL calculator, shows the result for both nuclear and coulombic interactions, while on blue, following the same procedure, only coulombic interactions are considered. As can be seen, values obtained from the OCA measurements overlap with the values from the ONERA measurements, once again indicating no annealing effects. All values obtained follow, a behavior that fits within both curves, i.e. the curve that considers nuclear and coulombic interactions and the curve that only considers coulombic interactions. This could mean that at higher irradiation energies, coulombic interactions play a greater role than nuclear interactions for these photodiodes.

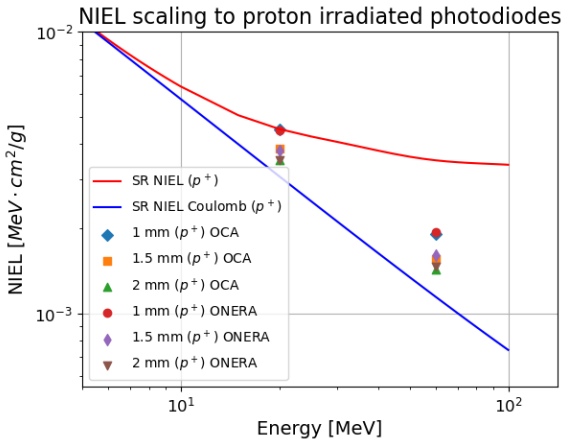

Figure 38: NIEL scaling approach applied to proton irradiated photodiodes.

Figure 39 shows the NIEL scaling approach applied to the electron irradiated photodiodes, considering measurements done with the setup from ONERA and with the setup from OCA. The curve in red shows the result from the SR NIEL calculation for electron irradiation on $In_{0.53}Ga_{0.47}As$, while the scattered symbols represent the NIEL value obtained from experimental damage factors applied to the NIEL scaling for each photodiode. It can be observed that for each respective photodiode diameter, the values measured at OCA provide a lower NIEL than the values measured at ONERA, indicating that there was annealing between the measurements. The values do not adhere completely to the SR NIEL curve but follows its behavior. A possible explanation for this is that there is not a proper distribution of Threshold displacement energies, as the values used by default come from GaAs [44] and $In_{0.49}Ga_{0.51}P$ [45]. Curves that fit the values can be found using more accurate threshold displacement energies [46].

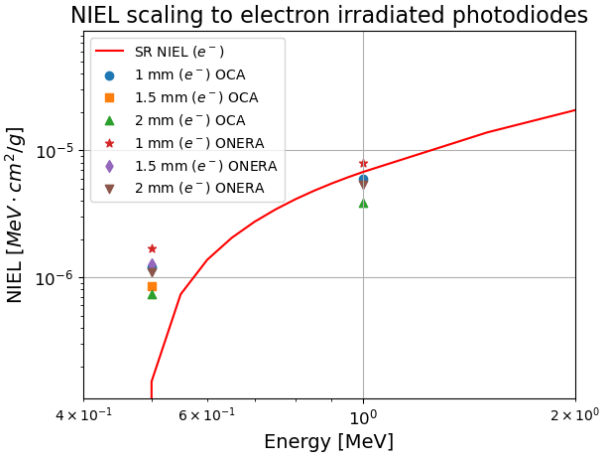

Figure 39: NIEL scaling approach applied to electron irradiated photodiodes.

5. Conclusions

In this project, a highly accurate IV-CV measurement setup was developed, and then used to measure the characteristics of irradiated and non-irradiated photodiodes which are candidates to be used for the LISA Mission. Such photodiodes have been developed by Hamamatsu in Japan from InGaAs with technologies to enhance their time response and reduce their capacitance, as well as make them more radiation resistant.

Proper shielding was applied to the CV measurement setup to reduce parasitic impedances, and a proper calibration method was implemented to compensate for the remaining parasitics of the test fixture. Also, appropriate connections were applied to the IV setup to ensure that the measurement of each quadrant of the photodiodes was not affected by the other quadrants. Calibration of the setup was done by repeating measurements with reference photodiodes and comparing results with measurements performed with an IV-CV setup from ONERA. Dark current precision measurements provided standard deviation to mean ratio of less than 4% while accuracy compared with measurements performed at ONERA gave values higher than 91%. CV measurements performed at ONERA did not provide good repeatability and therefore were not considered for further measurements.

IV measurements showed that there was a considerable increase in the dark current for the case of the proton irradiated photodiodes, although even after 1 year of irradiation there was no observed annealing effect. The electron irradiated photodiodes once again showed an increase in the dark current after irradiation and annealing after more than 500 days between measurements was observed, being the ratio of decrease of the dark current between the OCA and ONERA measurements at 5 V reverse bias to be around 40% for all photodiodes. The Gamma-ray irradiated photodiode had an annealing process preformed at ONERA in which its dark current already decreased, and no post annealing was observed from the measurements performed at OCA.

For the case of the CV measurements, slight increases in capacitance were observed for the irradiated photodiodes, being the largest difference 0.73 pF for the 2 mm 20 MeV proton irradiated photodiode. Differences between capacitances were so low and within standard deviations, that it is not possible to say if there was a real effect from irradiation on the capacitance of the photodiodes, which is what was expected as an increase in capacitance could seriously affect the detected signals by inducing jitter in the measurements.

Experimental damage factors from dark current were used to implement the NIEL scaling approach, showing a slight difference between the photodiode sizes for the same scaling factor, and a tendency which may be closer coulombic interactions at higher energies as compared to nuclear interactions. NIEL from proton irradiated photodiodes indicated once again no annealing, while annealing is visible for the electron irradiated photodiodes.

6. Future work

Improvements on the measurement setup can be done by implementing a system using a switching matrix or a system or relays which isolates the signal between the IV measurement setup and the CV measurement setup, so that a photodiode can be connected to a single fixture, and without having to interfere with it, be able to switch between IV and CV measurements, by controlling the switching matrix or the relays from an external control device such as a microcontroller.

Temperature stabilization using a climatic chamber, although accurate, is very slow, and it is important to perform many measurements in a short amount of time as many candidates will continue to be tested for the LISA Mission. Therefore, a temperature control system that can change the temperature of the photodiodes faster could make the process more efficient. To this end, A Peltier cell using PID control with a temperature sensor could be used, together with a metallic fixture in contact with the photodiodes so that temperature transfer is more efficient.

Applying structured annealing to the proton irradiated photodiodes such as the one used the gamma irradiated ones, and measuring their IV and CV characteristics as well as their damage factors and NIEL could help better understand the type of damage caused within the,

Photodiodes developed by the Netherlands (Bright Photonics and SMART Photonics industries) are another candidate for the LISA mission, which have also undergone irradiation procedures more than one year ago for proton and gamma irradiation. IV and CV characterization of these photodiodes with the present setup could help understand the annealing effects on these devices as well.

Future irradiation campaigns including also electron irradiation and further IV and CV measurements on the Netherlands' photodiodes over a period of time, could help better understand the annealing effects of electron irradiation on InGaAs photodiodes.

7. References

[1] H. Yu, Z. C. Lin, and Y. X. Liu, “Gravitational Waves and Extra Dimensions: A Short Review,” *Commun Theor Phys*, vol. 71, no. 8, pp. 991–1006, Aug. 2019, doi: 10.1088/0253-6102/71/8/991.

[2] R. A. Hulse and J. H. Taylor, “DISCOVERY OF A PULSAR IN A BINARY SYSTEM,” 1975.

[3] T. J.-L. Courvoisier, “The Hulse-Taylor Pulsar and Gravitational Radiation,” 2013, pp. 225–233. doi: 10.1007/978-3-642-30970-0_15.

[4] S. Yang and G. Zhang, “A review of interferometry for geometric measurement,” Sep. 04, 2018, *Institute of Physics Publishing*. doi: 10.1088/1361-6501/aad732.

[5] K. Riles, “Gravitational waves: Sources, detectors and searches,” Jan. 2013. doi: 10.1016/j.ppnp.2012.08.001.

[6] B. P. Abbott *et al.*, “Observation of gravitational waves from a binary black hole merger,” *Phys Rev Lett*, vol. 116, no. 6, Feb. 2016, doi: 10.1103/PhysRevLett.116.061102.

[7] M. Pitkin, S. Reid, S. Rowan, and J. Hough, “Gravitational Wave Detection by Interferometry (Ground and Space),” 2011. [Online]. Available: http://www.livingreviews.org/lrr-2011-5

[8] W. M. Folkner, P. L. Bender, and R. T. Stebbins, “LISA Mission Concept Study Laser Interferometer Space Antenna For the Detection and Observation of Gravitational Waves,” 1998.

[9] J. Camp and K. Numata, “Development of a US Gravitational Wave Laser System for LISA,” in *Journal of Physics: Conference Series*, Institute of Physics Publishing, May 2015. doi: 10.1088/1742-6596/610/1/012033.

[10] M. Otto, “Time-delay interferometry simulations for the laser interferometer space antenna,” 2015.

[11] Millinger Mark and Jiggens Piers, “LISA Environment Specification,” Noordwijk, Netherlands, Jun. 2020.

[12] C. Hu, *Modern semiconductor devices for integrated circuits*. Pearson India Education Services, 2010. Accessed: Aug. 05, 2024. [Online]. Available: https://cir.nii.ac.jp/crid/1130282272403171840.bib?lang=en

[13] R. H. Pratt, “Tutorial on fundamentals of radiation physics: Interactions of photons with matter,” in *Radiation Physics and Chemistry*, Jul. 2004, pp. 595–603. doi: 10.1016/j.radphyschem.2003.12.032.

[14] R. D. Evans, *The Atomic Nucleus*. N. Y.: McGraw-Hill, 1965.

[15] W. R. Fahrner, “Chapter 9 An overview of radiation-matter interactions,” *Instabilities in Silicon Devices*, vol. 3, no. C, pp. 553–637, Jan. 1999, doi: 10.1016/S1874-5903(99)80016-0.

[16] A. Karmakar, J. Wang, J. Prinzie, V. De Smedt, and P. Leroux, “A Review of Semiconductor Based Ionising Radiation Sensors Used in Harsh Radiation Environments and Their Applications,” *Radiation*, vol. 1, no. 3, pp. 194–217, Aug. 2021, doi: 10.3390/radiation1030018.

[17] J. S. George, “An overview of radiation effects in electronics,” in *AIP Conference Proceedings*, American Institute of Physics Inc., Oct. 2019. doi: 10.1063/1.5127719.

[18] W. L. Brown, W. M. Augustyniak, and T. R. Waite, “Annealing of radiation defects in semiconductors,” *J Appl Phys*, vol. 30, no. 8, pp. 1258–1268, 1959, doi: 10.1063/1.1735303.

[19] K. G. Libbrecht and E. D. Black, “A basic Michelson laser interferometer for the undergraduate teaching laboratory demonstrating picometer sensitivity,” *Am J Phys*, vol. 83, no. 5, pp. 409–417, May 2015, doi: 10.1119/1.4901972.

[20] B. P. Abbott *et al.*, “LIGO: The laser interferometer gravitational-wave observatory,” *Reports on Progress in Physics*, vol. 72, no. 7, 2009, doi: 10.1088/0034-4885/72/7/076901.

[21] M. Gehler, “LISA measurement concept justification document,” Noordwijk, Netherlands, May 2022.

[22] N. Storey, *Electronics: a systems approach*. Pearson Education, 2006.

[23] “Photodiode Basics,” https://www.teamwavelength.com/photodiode-basics/.

[24] O. Sergiyenko *et al.*, “Electromechanical 3D Optoelectronic Scanners: Resolution Constraints and Possible Ways of Improvement,” in *Optoelectronic Devices and Properties*, InTech, 2011. doi: 10.5772/14263.

[25] F. J. Effenberger and A. M. Joshi, “Ultrafast, dual-depletion region, InGaAs/InP p-i-n detector,” *Journal of Lightwave Technology*, vol. 14, no. 8, pp. 1859–1864, 1996, doi: 10.1109/50.532024.

[26] J. and P. J. Kaniewski, “InGaAs for infrared photodetectors. Physics and technology,” *Opto-Electron. Rev.*, vol. 12, no. 1, pp. 139–148, 2004.

[27] L. Olantera *et al.*, “Radiation Effects on High-Speed InGaAs Photodiodes,” *IEEE Trans Nucl Sci*, vol. 66, no. 7, pp. 1663–1670, Jul. 2019, doi: 10.1109/TNS.2019.2902624.

[28] N. Dharmarasu *et al.*, “High-radiation-resistant InGaP, InGaAsP, and InGaAs solar cells for multijuction solar cells,” *Appl Phys Lett*, vol. 79, no. 15, pp. 2399–2401, Oct. 2001, doi: 10.1063/1.1409270.

[29] C. Sah, R. Noyce, and W. Shockley, “Carrier Generation and Recombination in P-N Junctions and P-N Junction Characteristics,” *Proceedings of the IRE*, vol. 45, no. 9, pp. 1228–1243, Sep. 1957, doi: 10.1109/JRPROC.1957.278528.

[30] G. J. Shaw, R. J. Walters, S. R. Messenger, and G. P. Summers, “Time dependence of radiation-induced generation currents in irradiated InGaAs photodiodes,” *J Appl Phys*, vol. 74, no. 3, pp. 1629–1635, Aug. 1993, doi: 10.1063/1.354812.

[31] J. W. Walker and C. T. Sah, “Properties of 1.0-MeV-Electron-Irradiated Defect Centers in Silicon,” *Phys Rev B*, vol. 7, no. 10, pp. 4587–4605, May 1973, doi: 10.1103/PhysRevB.7.4587.

[32] M. Benfante, J.-L. Reverchon, C. Virmontois, S. Demiguel, and V. Goiffon, “Impact of Irradiation Temperature, Doping, and Proton Energy on InGaAs Photodiodes,” *IEEE Trans Nucl Sci*, vol. 71, no. 4, pp. 719–727, Apr. 2024, doi: 10.1109/TNS.2023.3340625.

[33] N. Dinu-Jaeger, “LISA QPD Irradiation tests report for TRA,” May 2023.

[34] S. Duzellier *et al.*, “AXEL lab.: Representative Ground Simulation for Investigating Radiation effects in Materials and Electronics,” in *2017 17th European Conference on Radiation and Its Effects on Components and Systems (RADECS)*, 2017, pp. 1–7. doi: 10.1109/RADECS.2017.8696228.

[35] “Test Facilities.” Accessed: Aug. 21, 2024. [Online]. Available: https://w3.onera.fr/nanosat/en/exp-facil/test

[36] P. Colcombet, “Étude de photorécepteurs sous irradiation de protons, électrons et rayons gamma pour la mission LISA,” 2024.

[37] Keysight, “Keysight Technologies Impedance Measurement Handbook A guide to measurement technology and techniques 4th Edition Application Note.”

[38] Q. Q. Lei *et al.*, “150 KeV proton irradiation effects on photoluminescence of GaInAsN bulk and quantum well structures,” *Opt Mater (Amst)*, vol. 97, p. 109375, Nov. 2019, doi: 10.1016/j.optmat.2019.109375.

[39] J. Ziegler, “Srim & trim, http://www.srim.org/.”

[40] A. Dalgarno, M. Yan, and W. Liu, “Electron Energy Deposition in a Gas Mixture of Atomic and Molecular Hydrogen and Helium,” *Astrophys J Suppl Ser*, vol. 125, no. 1, pp. 237–256, Nov. 1999, doi: 10.1086/313267.

[41] M. Boschini, P. Rancoita, and M. Tacconi, “SR-NIEL – 7 Screened Relativistic (SR) Treatment for NIEL Dose Nuclear and Electronic Stopping Power Calculator.” Accessed: Aug. 20, 2024. [Online]. Available: https://www.sr-niel.org/

[42] J. R. Srour and D. H. Lo, “Universal damage factor for radiation-induced dark current in silicon devices,” *IEEE Trans Nucl Sci*, vol. 47, no. 6, pp. 2451–2459, Dec. 2000, doi: 10.1109/23.903792.

[43] “Propagation of error.” Accessed: Aug. 20, 2024. [Online]. Available: https://academics.hamilton.edu/physics/smajor/courses/195Guides/phys190_uncertainties_II.pdf

[44] R. Campesato *et al.*, “NIEL Dose Analysis on triple and single junction InGaP/GaAs/Ge solar cells irradiated with electrons, protons and neutrons,” in *2019 IEEE 46th Photovoltaic Specialists Conference (PVSC)*, IEEE, Jun. 2019, pp. 2381–2384. doi: 10.1109/PVSC40753.2019.8980581.

[45] R. Campesato *et al.*, “Effects of irradiation on Triple and Single Junction InGaP/GaAs/Ge solar cells,” Sep. 2018.

[46] P. Colcombet *et al.*, “Radiation Tolerance of Low-Noise Photoreceivers for the LISA Space Mission,” *IEEE Trans Nucl Sci*, vol. 71, no. 8, pp. 1914–1923, Aug. 2024, doi: 10.1109/TNS.2024.3401047.